Graphical Abstract

Microstructure-Informed 3D Fractional Viscoelastic Modeling of Brain White Matter with Numerical treatment of Memory Effects

Parameshwaran Pasupathy, John G Georgiadis, Assimina A Pelegri

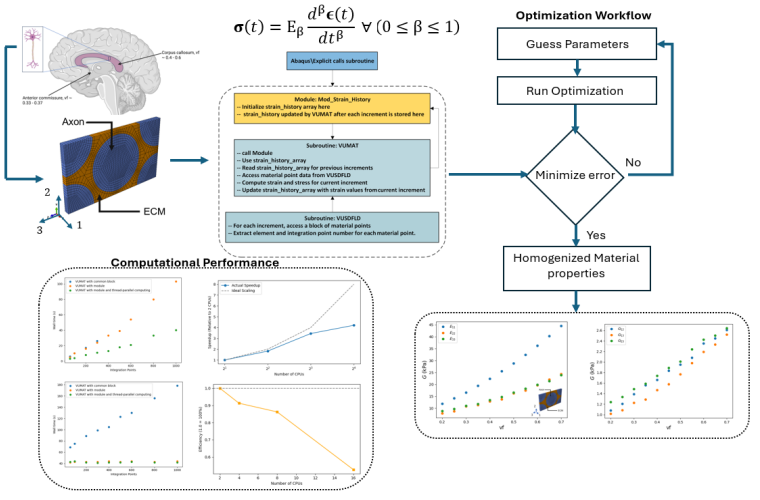

Highlights

Microstructure-Informed 3D Fractional Viscoelastic Modeling of Brain White Matter with Numerical treatment of Memory Effects

Parameshwaran Pasupathy, John G Georgiadis, Assimina A Pelegri

- Here, we develop and implement a 3D fractional viscoelastic model of BWM in the time domain for the first time.
- The directional mechanical response of the homogenized tissue can be characterized by two parameters: the generalized viscosity constant E_β, which governs the solid–fluid behavior, and a power-law exponent β, which encodes information about the underlying tissue architecture.
- The fractional viscoelastic model is numerically implemented using the Grünwald–Letnikov (GL) operator in a Fortran VUMAT subroutine and validated with benchmark examples.
- The results reveal the nonlinear variation of material parameters with axon volume fraction, the directional dependence of BWM mechanics, and the complex interplay among microstructural elements—all of which are crucial for understanding neuropathological changes associated with disease and aging.
- A closed-form analytical bound on the GL memory truncation error is derived, providing a principled basis for memory length selection.
- Significant computational gains are demonstrated through shared-memory parallelism, the short-memory principle, and modular strain history management.

Microstructure-Informed 3D Fractional Viscoelastic Modeling of Brain White Matter with Numerical treatment of Memory Effects

Parameshwaran Pasupathy[a], John G Georgiadis[b] and Assimina A Pelegri[a,*]

[a]Department of Mechanical and Aerospace Engineering, Rutgers, The State University of New Jersey, Piscataway, NJ, 08854, USA
[b]Department of Biomedical Engineering, Illinois Tech, Chicago, IL, 60616, USA

ARTICLE INFO

Keywords:
Brain white matter
fractional viscoelasticity
spring-pot
VUMAT
FEM

ABSTRACT

We present an explicit-dynamics 3D fractional viscoelastic finite element framework implemented via a modular Fortran VUMAT subroutine for the corpus callosum. Under linear viscoelasticity and causality, a frequency-domain power-law model yields a time-domain fractional constitutive update — a succinct, physically interpretable alternative to empirical Prony series. The framework is demonstrated through finite element (FE) homogenization of biphasic periodic representative volume elements: hexagonally packed axons embedded in an extracellular matrix under high strain-rate displacement-controlled loading. The model predicts that the generalized viscosity constant E_β varies linearly with volume fraction along the fiber direction and follows a bi-logistic function along the transverse normal and shear directions. The power-law exponent β exhibits a saturating exponential trend along the fiber direction and bi-logistic variation in the transverse and shear directions, revealing two distinct stiffening stages with increasing axonal content.

A closed-form analytical bound on memory truncation error is derived, enabling principled memory length selection. The thread-safe `VUMAT` implementation achieves up to an order-of-magnitude runtime reduction through modular strain history management, the short-memory principle, and shared-memory parallelism. This study presents, to our knowledge, the first explicit-dynamics 3D fractional viscoelastic FE implementation for brain white matter.

1. Introduction

Constituting approximately 50 percent of the human brain, white matter (BWM) plays a critical role in maintaining brain health, making it a key area related to diagnostics and therapeutics targeting the brain parenchyma. BWM contains billions of myelinated axons organized in 21 major tracts whose primary function is to facilitate communication between different brain regions [1]. Unlike other organs, such as the heart, for which robust prediction models backed by experiments and large scientific communities exist, mechanical characterization of the brain—particularly BWM—remains challenging.

Relating BWM response to external mechanical excitation requires a robust integration of biomechanical experiments and microstructural modeling. The above logical inference, however, belies the enormity of the task. Firstly, brain mechanics involves disparate scales, i.e., a highly compliant mechanical response under an applied load while being completely enclosed inside a hard skull. This makes the brain parenchyma hard to probe. Further complications in experimentation arise from the fact that the mechanical properties of brain tissue are highly multiphasic and region-specific. The large scatter of data and variations in results between *in vitro* experimental results and *in vivo* measurements are a testament to this fact, all before considering diverse factors such as gender, age, disease, past injury/trauma [2, 3, 4].

Additionally, axon concentration, thickness, distribution and orientation vary widely from region to region making BWM highly heterogenous and anisotropic (1). For instance, within the corona radiata, the axons that propagate outward are highly tortuous with lower volume fractions, whereas in the corpus callosum (CC), they are aligned and densely packed. Moreover, material characterization of BWM, even under the limit of small strains is difficult owing to its dependence on both magnitude and rate of strain. Quantifying this heterogeneity in BWM is therefore critical for addressing a wide range of questions related to aging, disease onset, and progression [5]. In light of the above considerations, this study focuses on developing computational models that describe the viscoelastic material

*Corresponding author
pelegri@rutgers.edu (A.A. Pelegri)
ORCID(s):

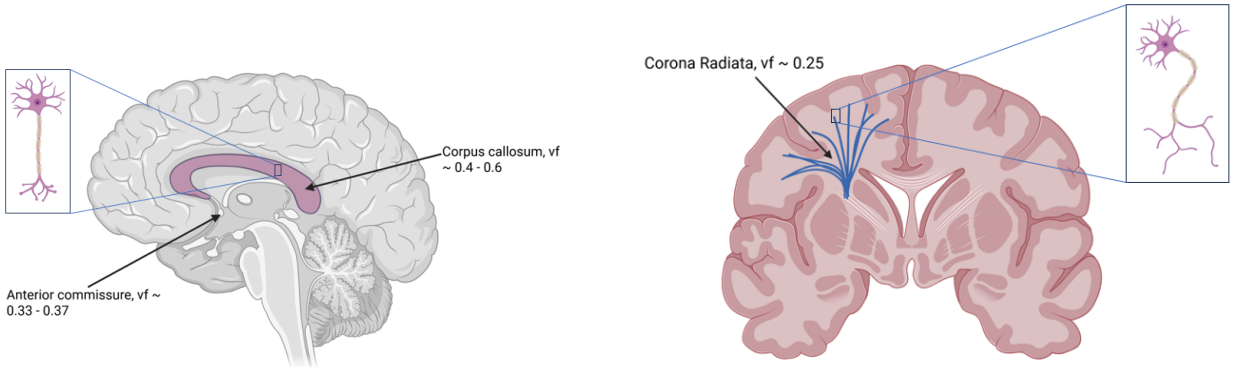

Figure 1: A schematic representation of the brain examined through different cut planes [10]. (a) Sagittal cut of the brain depicting the CC of the brain containing aligned myelinated axons with volume fraction (vf): 0.4 - 0.6 [8] and, anterior commissure, vf: 0.33 - 0.37 [11]. (b) Coronal cut depicting white matter and corona radiata containing highly tortuous myelinated axons propagating outward with a vf: $\approx$ 0.25 [12].

response of BWM under mechanical loading, with particular focus on regions with aligned axonal bundles, where such models are most appropriate.

The past two decades have seen significant progress in *in vivo* and *ex vivo* mechanical characterization of BWM, with growing evidence indicating that axonal damage is the leading cause of traumatic brain injury (TBI), with excessive tensile strain postulated as the underlying mechanism [6]. Moreover, diffuse axonal injury, which leads to impaired consciousness in patients, occurs due to the shearing of axons [7], highlighting the importance of characterizing the mechanical response of myelinated axon bundles in BWM with high fidelity.

In vivo magnetic resonance imaging (MRI) has allowed the estimation of microstructural parameters related to the spatial distribution of axons in BWM. In particular, diffusion-based MRI techniques have been used to quantify mean axonal diameter, inter-axonal volume fraction, and axon density across healthy young, and aging brains. Studies report that in healthy adults, the mean axon diameter is larger in the body of the CC and smaller in the genu and splenium, whereas the opposite trend was observed for the inter-axonal volume fraction [8]. In aging brains, a global increase in axon diameter index and a decrease in packing density throughout the CC has been observed with the effect being most pronounced in the genu [9].

The advent of elastography (MRE), coupled with *ex vivo* experiments and modeling techniques such as the finite element method, molecular dynamics, and more recently, machine learning, has yielded promising results for *in vivo* characterization of BWM. Researchers using MRE have observed wide variations in region-specific mechanical properties of BWM compared to global white matter properties [13]. Moreover, MRE-based studies have documented significant degradation of BWM mechanical properties in patients with multiple sclerosis [14], as well as disability-associated effects that appear independent of disease duration [15].

Several computational models of the microstructure of BWM, based on structure–property relationships gleaned from MRI/MRE, have been proposed. These span triphasic unidirectional composite models, consisting of axons, myelin, and extracellular matrix (ECM), which estimate homogenized viscoelastic properties under steady-state oscillatory dynamics [16], to single-axon models with substructure resolutions under varying strain rates, investigating axonal injury mechanisms [17]. A number of these studies use Prony series models for viscoelastic material characterization in the time domain. Javid et al. [18] used the genetic algorithm optimization procedure to determine the homogenized Prony series parameters for representative volume elements (RVEs) of axons in the ECM. The objective function was defined using relaxation tests performed on the porcine brain white matter. A microstructure-informed finite element model with an Ogden hyperelastic strain energy density function and a two term Prony series viscoelastic model under cyclic loading developed by Reiter et al. [19] observed that viscoelastic time constants are transferable between porcine and human brain tissue. Li et al. [20] estimated the linear viscoelastic material properties of grey and white matter of bovine brain tissue through a Prony series model under compression loading. An MRI–based FEM model of a mouse brain coupled with a convolutional neural network (CNN) algorithm for cortical impact simulations

was developed by Lai et al. [21]. The anatomical details were mapped to each FEM element from the corresponding image voxel. A CNN network was used to reconstruct strain-maps from FEM data. Wu et al. [22] developed a multiscale 3D residual neural network algorithm that utilizes a voxelization method to obtain geometry information from 3D RVEs that are based on MRI/MRE data. The architecture information is then encoded in the voxelized location while cross-referencing the RVEs' material properties.

Viscoelastic material characterization via Prony series can replicate phenomenological behavior; however, its physical interpretation is often challenging. Even a simple two-parameter Prony series model requires the estimation of five material constants. A number of research studies indicate that the viscoelastic response of BWM can be phenomenologically explained by a power-law behavior. Studies employing multifrequency MRE fitted to a power-law model have characterized age-related alterations in BWM [4, 23] and the impact of neuroinflammation on brain viscoelastic properties during the early stages of multiple sclerosis [24]. Kurt et al. [25] developed a protocol to calculate optimal frequency sets and determine power-law parameters separately for the entire brain, white matter and grey matter. Clayton et al. [26] used MRE to probe the mouse brain tissue across a 1200 Hz bandwidth (600-1800 Hz) and observed that the complex modulus is well approximated by the power-law. Using ultrasound shear wave elastography, Nicolas et al. [27] performed *ex vivo* brain experiments and determined its mechanical parameters by fitting a power-law model. Kang et al. [28] used a power-law model to describe the creep and relaxation profiles of adult porcine white and gray matter under uniaxial compression tests. Mishra and Cleveland [29] conducted low-frequency oscillatory shear tests to measure the rheological properties of porcine organs, including the brain, and developed the Semi-Fractional Kelvin–Voigt model to characterize their mechanical response.

It is well established that both geometric and dynamic self-similarity, as well as scale invariance, are prominently expressed in the brain [30]. Building on this finding, we posit in the present that the viscoelastic power-law behavior observed at the tissue level extends across length scales—from the continuum macroscopic level to the microstructural realm of the axons—and across a range of frequencies. A viscoelastic power-law model of a spring-pot is applied to the axons and the ECM. The material parameters for the spring-pot are obtained through a linear regression analysis. A 3D fractional viscoelastic model is then implemented within the finite element framework. Homogenized fractional viscoelastic parameters as a function of the volume fractions of axons embedded in the ECM are finally derived [31].

2. Methods

Figure 2 illustrates the workflow of implementing the fractional viscoelastic model for BWM. The remainder of this article essentially delves into each component of the model. Section 2.1 describes the linear regression model for estimating power-law parameters of the microstructure of BWM. The implementation, validation and homogenization of the fractional viscoelastic model are discussed in section 2.2 — section 2.7. The results are documented and discussed in section 3 and section 4.

2.1. Linear Regression Model for Power-Law

The stress-strain response for a viscoelastic material at time t with the action of stress beginning at time τ can be described using a convolution integral of the form

$$\sigma(t) = \int_0^t G(t-\tau)\frac{d\epsilon(\tau)}{d\tau}\,d\tau, \tag{1}$$

and the strain as a function of stress is determined by

$$\epsilon(t) = \int_0^t J(t-\tau)\frac{d\sigma(\tau)}{d\tau}\,d\tau, \tag{2}$$

where $G(t-\tau)$ and $J(t-\tau)$ are the relaxation and creep modulus of the material, respectively. In the frequency domain, the relaxation modulus can be expressed as a complex modulus G^* at a specified frequency ω, given by:

$$G^*(\omega) = G'(\omega) + iG''(\omega), \tag{3}$$

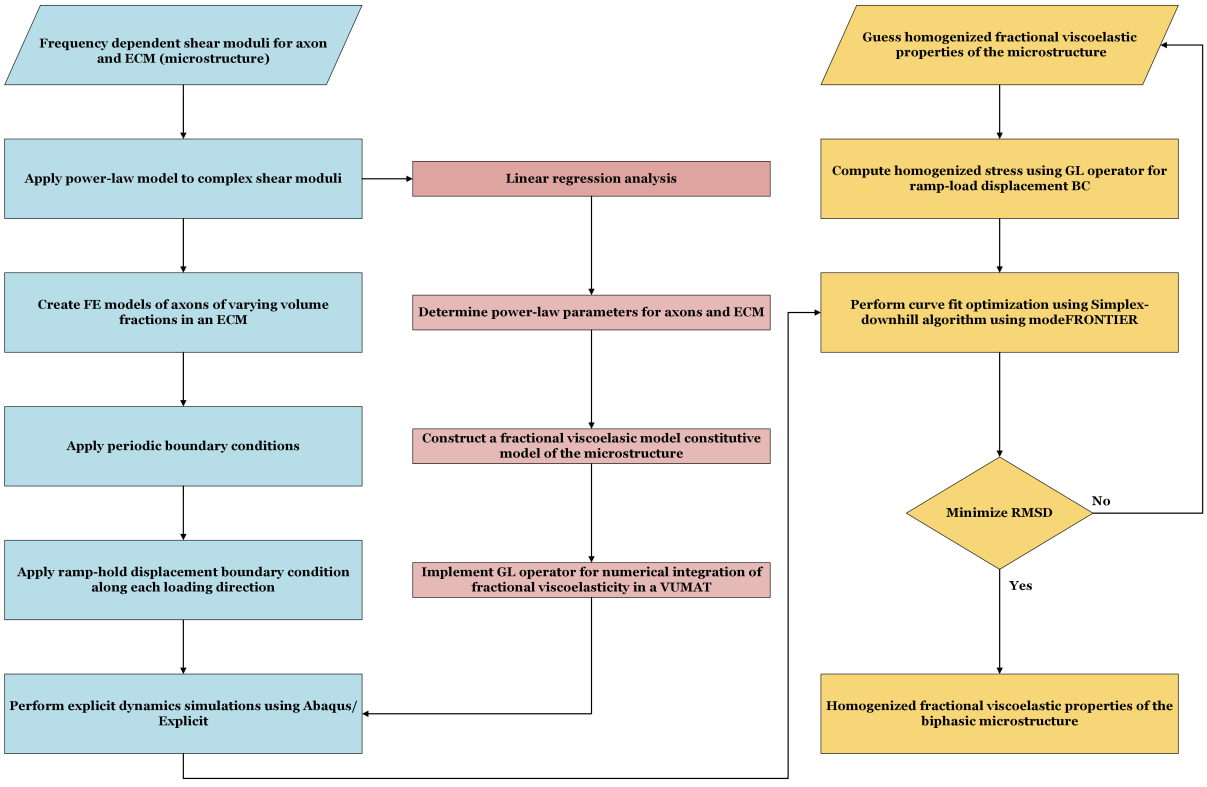

Figure 2: An algorithmic workflow for developing a fractional viscoelastic model of 3D biphasic unit cells representing axon and glia.

where G' is the storage modulus, a measure of the material's stiffness, and G'' is the loss modulus, related to the viscous dissipation of energy due to deformation. The complex modulus, when described by a power-law, with constants κ and β, is given by

$$G(\omega) = \kappa(i\omega)^{\beta} \tag{4}$$

A power-law model of the microstructure of brain white matter (BWM), comprising axons and an ECM, is obtained by fitting the model to experimentally measured shear moduli from oscillatory tests on the porcine optic nerve [32, 33].

$$\Re(G_{exp}(\omega)) + i\Im(G_{exp}(\omega)) = \kappa(i\omega)^{\beta} \tag{5}$$

The power-law parameters for the axon and ECM are obtained by transforming eq. (5) into the logarithmic domain and applying linear regression. This is accomplished by defining a cost function in the form,

$$E = \frac{1}{2m}\sum_{m}(\ln(\kappa) + \beta\ln(\omega) - \ln(|G_{exp}(\omega)|))^2 + \ (\beta\frac{\pi}{2} - \mathrm{Arg}(G_{exp}(\omega))))^2, \tag{6}$$

where E is the cost function and, m is the number of input frequency points. The cost function is minimized with respect to $\ln(\kappa)$ and β. The log-transformation linearizes the model and makes gradient descent optimization numerically more stable. The cost function is minimized with respect to $\ln(\kappa)$ and β.

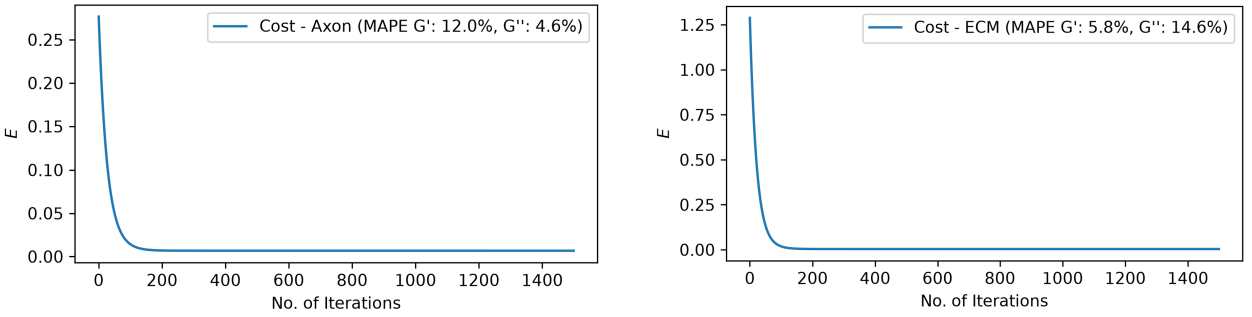

Figure 3: Evolution of the cost function over iterations for determining the power-law model parameters for (a) axons and (b) ECM.A total of 1500 iterations were performed to ensure convergence and stability of the minimization process.

Table 1
Power-law model parameters for axon and ECM components.

Component	$\kappa(Pa \cdot s^{\beta})$	β
Axon	264.115	0.419
ECM	252.503	0.239

$$\begin{aligned}\frac{\partial E}{\partial \ln(\kappa)} &= \frac{1}{m}\sum_{m}(\ln(\kappa) + \beta\ln(\omega) - \ln(|G_{exp}(\omega)|)) \\ \frac{\partial E}{\partial \beta} &= \frac{1}{m}\sum_{m}((\ln(\kappa) + \beta\ln(\omega) - \ln(|G_{exp}(\omega)|))\ln(\omega) + \frac{\pi}{2}(\frac{\beta\pi}{2} - \mathrm{Arg}(G_{exp}(\omega))))\end{aligned} \tag{7}$$

The parameters $\ln(\kappa)$ and β are updated simultaneously during each iteration as shown below. The learning rates γ_1 and γ_2 are adjusted through trial and error.

$$\begin{aligned}\ln(\kappa) &:= \ln(\kappa) - \gamma_1\frac{\partial E}{\partial \ln(\kappa)} \\ \beta &:= \beta - \gamma_2\frac{\partial E}{\partial \beta}\end{aligned} \tag{8}$$

The minimization of the cost function is shown in Figure 3. The power-law parameters for the axon and ECM are listed in Table 1. It can be observed that the axon is stiffer and more viscous than the ECM [6, 32]. The ECM, with a lower β, is softer than the axon (smaller κ) and behaves more like an elastic solid. The axon, being stiffer and more frequency-sensitive than the ECM, sustains a greater amount of stress under dynamic loading, making it particularly vulnerable to mechanical damage.

2.2. Governing Equations

In the time domain, a power-law model with constants A_β and β can be expressed as,

$$G(t) = A_\beta t^{-\beta} \tag{9}$$

Substituting eq. (9) into eq. (1), we obtain the following,

$$\sigma(t) = \int_0^t A_\beta(t-\tau)^{-\beta}\frac{d\epsilon(\tau)}{d\tau}\,d\tau \tag{10}$$

Equation (10) is of a form commonly encountered in the field of fractional calculus and is known as the Riemann–Liouville integral. It represents one of the most widely used definitions of the fractional derivative. Consider the function $u(t)$. Repeated integration of $u(t)$, performed $\beta \in \mathbb{R}$ number of times, can be expressed using Cauchy's integral formula as:

$$\begin{aligned} I^{\beta}u(t) &= \int_0^t \int_0^t \int_0^t ...u(t)\, dt^{\beta} \\ &= \frac{1}{\Gamma(\beta)} \int_0^t (t-\tau)^{\beta-1} u(\tau)\, d\tau, \end{aligned} \tag{11}$$

where $I^{\beta}\{\cdot\}$ denotes repeated integration over β number of times, $\Gamma(\beta)$ is the Gamma function. If the RHS of eq. (10) is set to $f(\tau)$, where $f(0) = 0$, then differentiating $f(\tau)$, β number of times yields the original function, $u(\tau)$.

$$\begin{aligned} f(\tau) &= \frac{1}{\Gamma(\beta)} \int_0^t (t-\tau)^{\beta-1} u(\tau)\, d\tau, \\ u(\tau) &= D^{\beta} f(\tau), \end{aligned} \tag{12}$$

where $D^{\beta}\{\cdot\}$ denotes differentiation by order β, a non-integer value. Performing a Laplace transform of eq. (12) yields $\frac{U(s)}{s^{\beta}} = F(s)$. Rewriting the expression as $U(s) = s(\frac{F(s)}{s^{(1-\beta)}})$ and then taking the inverse Laplace transform followed by integrating by parts, we obtain:

$$D^{\beta} f(t) = \frac{1}{\Gamma(1-\beta)} \int_0^t (t-\tau)^{-\beta} \frac{df(\tau)}{d\tau}\, d\tau \tag{13}$$

Comparing eq. (10) and eq. (13), the viscoelastic stress can be written as,

$$\sigma(t) = C_{\beta} D^{\beta} \epsilon(t) \tag{14}$$

where $C_{\beta} = A_{\beta}\Gamma(1-\beta)$.Taking the Laplace transform of eq. (10) yields $G(s) = \frac{sA_{\beta}}{s^{1-\beta}}$, where $G(s)$ is the shear modulus in the Laplace domain. Considering the analytical form of the Laplace and Fourier transforms,

$$\begin{aligned} \mathcal{L}[G(t)] = G(s) &= \int_0^{\infty} G(t) e^{-st}\, dt, \\ \mathcal{F}[G(t)] = G(\omega) &= \int_{-\infty}^{\infty} G(t) e^{-i\omega t}\, dt, \end{aligned} \tag{15}$$

and given $G(t)$ is causal, i.e. $G(t) = 0 \;\; \forall \;\; t < 0$, $\mathcal{L}[G(t)]$ exists with a region of convergence that includes the imaginary axis, the Laplace and Fourier transform are related via the imaginary unit $i = \sqrt{-1}$. Therefore, s can be interchanged with $i\omega$, where ω is the frequency in rad/s. This implies, from eq. (4) and eq. (15), that $C_{\beta} = \kappa$.

2.3. Fractional Viscoelastic Constitutive Material Model

Given that the stress is proportional to the zeroth order derivative of strain in an elastic spring and to its first order derivative in a dashpot, G.W. Scott Blair posited an intermediate material—between a Hookean solid and a Newtonian fluid—in which the stress is proportional to non-integer order of strain [34, 35, 36]. The mechanical response of such a "spring-pot" can be described by employing the Riemann-Liouville integral in eq. (10) and, eq. (14) as [37, 38, 39, 40]:

$$\begin{aligned} \sigma(t) &= \kappa \frac{d^{\beta}\epsilon(t)}{dt^{\beta}} \\ &= \frac{\kappa}{\Gamma(1-\beta)} \int_0^t (t-\tau)^{-\beta} \frac{d\epsilon(\tau)}{d\tau}\, d\tau \qquad\qquad \forall\ (0 \le \beta \le 1) \end{aligned} \tag{16}$$

The fractional spring-pot model for the microstructure of BWM is implemented in three dimensions using the finite element method in Abaqus software. In 3-dimensions, the relaxation matrix can be split into its volumetric and deviatoric components [41],

$$G_{ijkm}(t) = (K_R(t) - \frac{2}{3}G_R(t))\delta_{ij}\delta_{km} + G_R(t)(\delta_{ik}\delta_{jm} + \delta_{im}\delta_{jk}), \tag{17}$$

where δ_{ij} is the Kronecker delta function. $G_R(t)$ and $K_R(t)$ are the deviatoric and volumetric power-law functions respectively. Substituting eq. (17) into eq. (16) and rewriting terms of the power-law coefficient κ, in terms of the volumetric and deviatoric components, K_β and G_β, the stress-strain equation becomes,

$$\sigma_{ij} = \frac{1}{\Gamma(1-\beta)}\int_0^t (t-\tau)^{-\beta}(K_\beta - \frac{2}{3}G_\beta)\delta_{ij}\dot{\epsilon_{kk}}(\tau)\,d\tau + \frac{1}{\Gamma(1-\beta)}\int_0^t G_\beta(t-\tau)^{-\beta}(\dot{\epsilon_{ij}}(\tau) + \dot{\epsilon_{ji}}(\tau))d\tau \tag{18}$$

For any function $f(x)$ containing β order continuous derivatives, the fractional derivative of $f(x)$ can be computed by the Grünwald–Letnikov (GL) operator which is given by [42, 43],

$$\frac{d^\beta f(x)}{dx^\beta} = \lim_{n\to\infty}(\frac{n}{x})^\beta \sum_{l=0}^{n}(-1)^l \frac{\Gamma(\beta+1)}{\Gamma(\beta+1-l)l!} f(x - \frac{l}{n}x) \tag{19}$$

Under weak conditions imposed on $f(x)$ as described above, the Riemann-Liouville integral is equivalent to the GL definition of the fractional derivative. Alotta et al. [44] implemented a 3D fractional viscoelastic user material (`UMAT`) subroutine in Abaqus using the GL operator. For a 3D state of stress, $\sigma(t) = [\sigma_{11}\ \sigma_{22}\ \sigma_{33}\ \tau_{23}\ \tau_{31}\ \tau_{12}]$, the stress in any direction for eq. (18) can be obtained by its GL equivalent as,

$$\sigma_{ij}^{k+1} = (K_\beta - \frac{2G_\beta}{3})\left(\frac{1}{\Delta t}\right)^\beta \sum_{l=1}^{k+1}\varphi_l\epsilon_{kk}((k+1-l)\,\Delta t) + 2G_\beta\left(\frac{1}{\Delta t}\right)^\beta \sum_{l=1}^{k+1}\varphi_l\epsilon_{ij}((k+1-l)\Delta t), \tag{20}$$

where $k = \frac{t}{\Delta t}$ is the number of iterations, t is the current simulation time, ϵ_{kk} is the volumetric strain, and ϕ_l are the Grünwald coefficients used to handle the gamma functions in eq. (19), which can be computed as described in [45] as,

$$\varphi_{l+1} = \frac{(k-1-\beta)}{k}\varphi_l, \qquad \varphi_1 = 1. \tag{21}$$

Equation (20) is implemented in Abaqus through a vectorized Fortran user material subroutine `VUMAT` (Algorithm 1), which is specifically used for explicit time integration. Note that the calculation of stress for any given increment requires storing and accessing the history of strains for all previous increments. This makes the simulation of large models using an explicit integration scheme computationally expensive. The `VUMAT` is invoked multiple times by the solver during each increment as it processes blocks of material points. For each material point, the strain history must be indexed, stored, and retrieved based on the corresponding element number and integration point.

2.4. Finite Element Model

The FE model of the microstructure of BWM is constructed by assuming a periodic distribution of hexagonally packed axons embedded in an ECM as shown in Figure 4. The diameter of the axon in the RVE is 10 μm. The volume fraction is varied in steps of 0.05 from 0.2 to 0.7. Periodic boundary conditions (PBC) are applied to the hexagonally packed structure. PBC is imposed on the nodes of the model through a set of linear constraint equations in Abaqus [46, 47]. The far-field gradient is applied through the degrees of freedom of reference points (RP) using the following equation [48],

$$u_i(x_j + p_j^\alpha) = u_i(x_j) + \frac{\partial u_i}{\partial x_j}p_j^\alpha, \tag{22}$$

Algorithm 1 VUMAT: Fractional Grünwald–Letnikov Operator

Require: Material name and props (λ, μ, β)
Module StrainHistory:
$\mathcal{H}[N_{steps}, N_{elem}, N_{pt}, N_{dir}]$ ▷ Allocate viscoelastic memory
Step 1: Global Context (Dispatcher)
if *cmname* == 'Material Prop' **then**
Call Vumat_GL ▷ Execute Fractional Operator logic
else
return
end if
end subroutine Vumat
Step 2: Initialization (Inside Vumat_GL)
Require: $n_{block}, n_{dir}, n_{shr}, n_{statev}, n_{props}, \Delta t, t, \boldsymbol{\sigma}^{old}, \boldsymbol{\varepsilon}^{old}, \Delta\boldsymbol{\varepsilon}$
use StrainHistory, only: $\mathcal{H}$
Define Memory length = M
$k \leftarrow \lfloor t/\Delta t \rfloor$ ▷ Current temporal index
$k_{red} \leftarrow \lfloor M/\Delta t \rfloor$ ▷ Short Memory time index
if $k \leq k_{red}$ **then**
$k_{red} = k$
end if
$A_1 \leftarrow 1, \quad A_{\ell+1} \leftarrow A_\ell \frac{\ell-\beta-1}{\ell}$ **for** $\ell = 1 \ldots k$
Step 3: Vectorized Block Processing
for $i = 1$ **to** n_{block} **do**
$ID \leftarrow j_{elem}(i)$ ▷ Global element mapping
$IP \leftarrow k_{npt}$ ▷ Integration point index
Update Strain History:
$\boldsymbol{\varepsilon}_i^{curr} \leftarrow \boldsymbol{\varepsilon}_i^{old} + \Delta\boldsymbol{\varepsilon}_i$ ▷ Update strain vector
$\mathcal{H}[k+1, ID, IP, 1:6] \leftarrow \boldsymbol{\varepsilon}^{curr}$
$\boldsymbol{\varepsilon}^{prev} = \mathcal{H}[k, ID, IP, 1:6] \leftarrow \boldsymbol{\varepsilon}^{curr}$ ▷ Read strain history
Initialize stress for current increment
$W \leftarrow A_1/\Delta t^\beta$
$I_e \leftarrow \text{trace}(\boldsymbol{\varepsilon}_{curr})$
$\sigma_k \leftarrow W \cdot (\lambda I_e \mathbf{1} + 2\mu\boldsymbol{\varepsilon}_{curr})$
for $\ell = 1$ **to** k_{red} **do**
$W \leftarrow A_{\ell+1}/\Delta t^\beta$
$I_e \leftarrow \text{trace}(\boldsymbol{\varepsilon}_{hist}(k+1-l))$
$\sigma_k \leftarrow \sigma_k + W \cdot (\lambda I_e \mathbf{1} + 2\mu\boldsymbol{\varepsilon}_{hist}(k+1-l))$
end for
$\boldsymbol{\sigma}^{new} \leftarrow \boldsymbol{\sigma}_k$
end for
end subroutine Vumat_GL
Subroutine VUSDFLD
Require: $n_{block}, n_{props}, n_{statev}, state_{New}(n_{block}, n_{statev})$, *cmname*
for $i = 1$ **to** n_{block} **do**
$state_{New}(i, n_{statev}) \leftarrow j_{elem}(i)$ ▷ Update statev corresponding to element number
$state_{New}(i, n_{statev}) \leftarrow k_{npt}(i)$ ▷ Update statev corresponding to element int point
end for
end subroutine VUSDFLD

where x_j is a nodal coordinate, p_j^α is the αth vector of periodicity, and $\frac{\partial u_i}{\partial x_j}$ is the far-field gradient of the displacement. RP nodes are not physically connected to any elements in the model. However, the equivalent internal force response in a given direction can be obtained by extracting the reaction forces at a prescribed RP. To correctly apply PBC, it is essential that the mesh on each pair of opposite faces is identical. This allows the desired field variable at x_j to be paired with its counterpart $x_j + p_j^\alpha$ on the opposing face when formulating the linear constraint equations [48, 49] shown below

$$A_1 u_i^p + A_2 u_j^q + \cdots + A_n u_s^v = 0, \tag{23}$$

where n is the number of terms in the equation, u_i^P is the displacement variable at node P and degree of freedom i, and A_n are the coefficients.

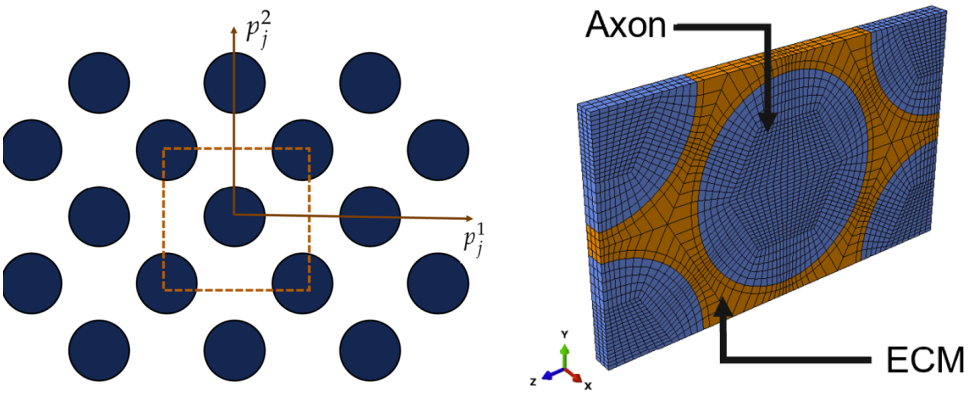

(a) (b)

Figure 4: (a) A schematic of a periodic geometry of axons in an ECM. (b) A FE model of the hexagonally packed RVE of two axons embedded in an ECM.

The finite element model of the RVE, incorporating the fractional viscoelastic `VUMAT`, is subjected to a ramp-hold displacement boundary condition along six loading directions with a maximum strain of 0.5%. A Poisson's ratio of $\nu = 0.3$ is adopted in this study, consistent with values as low as 0.33 reported in prior experimental and computational studies [50, 51]. A broader sensitivity analysis examining Poisson's ratio values in the range $0.3 \leq \nu \leq 0.45$, spanning the near-incompressible behavior of brain tissue, is currently ongoing and will be reported in a future study. An explicit time integration scheme is used to solve the model. A conservative stable time increment of 4.5×10^{-6} ms, derived from the CFL limit, is held fixed across all volume fractions and loading directions. The time increment is held fixed because the strain history arrays, allocated at model initialization, assume uniform temporal spacing for the purpose of storing and retrieving strain histories. Automatic incrementation would require dynamic remapping of the fractional memory.

The simulation is conducted over a total time of 0.2025 ms, comprising a ramp to peak strain over $t_{ramp} \approx 0.04\ ms$ followed by a hold phase. This corresponds to a strain rate of 123.5 s^{-1} consistent with the high-frequency end of the documented power-law behavior of brain white matter. The power-law model, unlike Prony series models with discrete relaxation times, describes a continuous distribution of relaxation processes across time scales [37], making it applicable over a broad frequency range. Brain white matter has been shown to exhibit power-law behavior extending into the kHz range [26], and fractional viscoelastic models have been validated for soft tissue-mimicking phantom materials at frequencies up to 16 kHz [52, 53], supporting the applicability of the fractional viscoelastic model at the time scales used in this study.

2.5. Model Validation

The `VUMAT` subroutine is tested and validated using a set of benchmark problems with known analytical solutions. We first apply the model to a single element unit cube under uniaxial stretch (Figure 5a) and shear (Figure 5b). The material properties for the cube are based on a test case developed by Alotta et al [44, 54]. For a quasi-static displacement boundary condition, such as a uniaxial stretch, the strain can be written in terms of a unit-step function as,

$$\begin{aligned} \epsilon_{11} &= \bar{\epsilon}\,[t\mathcal{H}(t) - (t-1)\mathcal{H}(t-1)] \\ \epsilon_{22} &= \epsilon_{33} = 0 \end{aligned} \tag{24}$$

where $\bar{\epsilon}$ is a scalar and $\mathcal{H}(t)$ is the Heaviside function. In this case, the quasi-static boundary condition is applied such that the strain increases linearly with time until $t = 1s$, after which it remains constant (see Figure 5c). The time-derivative of strain is a rectangular pulse in the interval $t \in [0, 1]s$. By substituting eq. (24) in eq. (18), the stress along the direction of the stretch is obtained as,

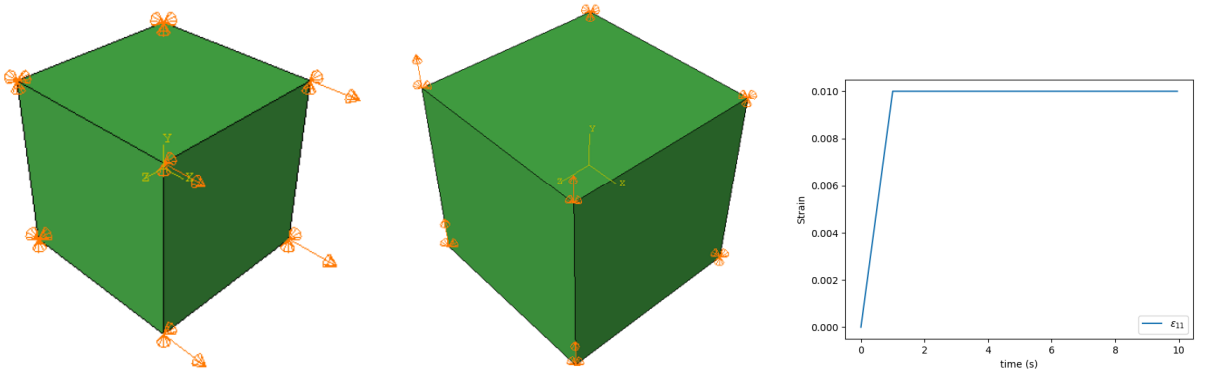

(a) (b) (c)

Figure 5: Benchmark testing of the `VUMAT` subroutine using a unit cube model. (a) Unit cube subjected to a quasi-static tensile stretch as described in (c). (b) Unit cube subjected to a quasi-static shear deformation as described in (c). (c) Quasi-static strain loading profile applied to (a) and (b), with an amplitude of 1%.

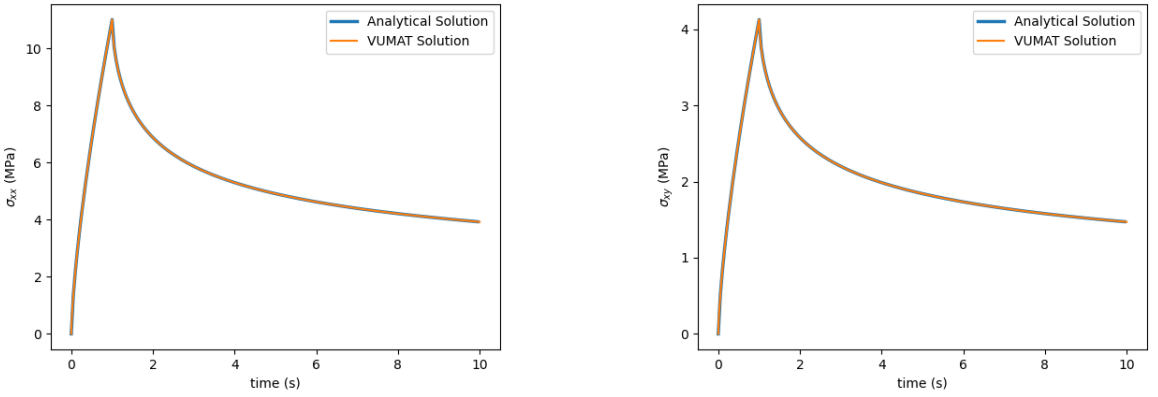

(a) (b)

Figure 6: Comparison of the `VUMAT` subroutine with analytical solution for a unit cube model under a quasi-static strain with a peak amplitude of 0.01. (a) Uniaxial stress response. (b) Shear stress response.

$$\sigma_{11} = \frac{\bar{\epsilon}}{\Gamma(1-\beta)}\left(K_\beta + \frac{4G_\beta}{3}\right)\left[t^{(1-\beta)}\mathcal{H}(t) - (t-1)^{(1-\beta)}\mathcal{H}(t-1)\right] \tag{25}$$

The comparison between the analytical solution and the `VUMAT` subroutine is shown in Figure 6a. The shear stress response under a pure-shear type displacement is shown in 6b. Next, a plate with a hole is subjected to a uniform tensile load of 2 MPa held constant for $t = 5$s. The evolution of the tensile strain in the plate computed via the `VUMAT` implementation is compared with the `UMAT` subroutine developed by Alotta et al [44] (see Figure 7).

Typically, the size of the RVE must be large enough to adequately represent the macroscale behavior. However, in practice, the size, specifically the thickness of the RVE along the fiber direction is not always obvious. In a hexagonally packed structure, given the volume fraction and the fiber radius, the cross-sectional area of the RVE becomes fixed. When periodic boundary conditions are applied, the strain field is uniform along the fiber direction and is independent of the thickness of RVE. However, the same cannot be said for the other loading directions. While RVE's with insufficient depth may fail to capture the mechanical behavior, excessively thick RVEs significantly increase computational cost without necessarily providing additional insight. In order to determine the optimal size of the RVE,

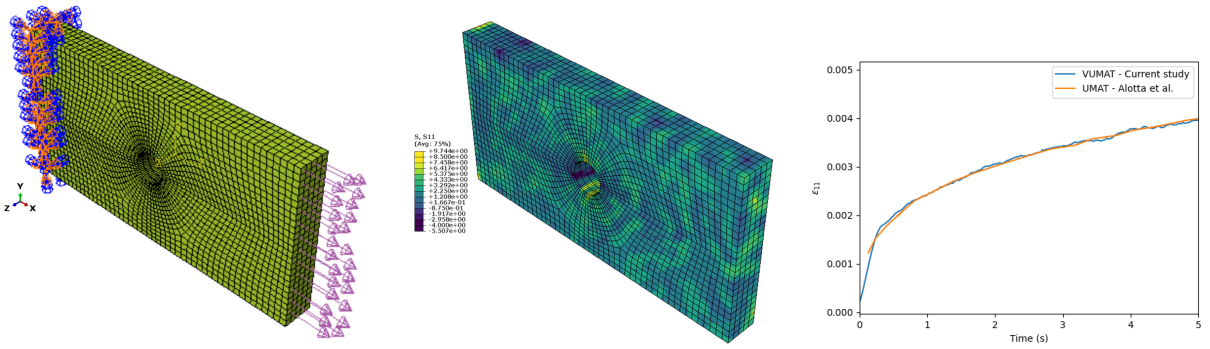

(a) (b) (c)

Figure 7: Benchmark testing of the `VUMAT` subroutine using a plate-with-a-hole model under uniaxial tension. (a) Finite element model constrained on the left end with a uniform tensile load of 2MPa applied on the right. The model contains 8720 C3D8R elements (Hexahedral elements with reduced integration.) (b) Fringe plot of the stress distribution, σ_{11} at $t = 5s$. (c) Comparison of the evolution of tensile strain with time in the solid model between the `VUMAT` solution implemented in the current study and the `UMAT` subroutine developed by Alotta et al [44].

Table 2
Summary of RVE depths and element types tested for determining the optimal RVE size. The 10 μm mesh is taken as the reference for NRMSD computation

RVE Thickness (μm)	Element Type	Number of Elements	NRMSD %	
			σ_{22}	σ_{13}
1	C3D8R	1952	6.10	–
1	C3D8	1952	6.13	7.25
2	C3D8	3904	2.56	3.71
3	C3D8	5856	1.95	2.37
10	C3D8R	9760	–	–

we consider different depths, number of elements and integration points shown in Table 2 for a volume fraction, vf = 0.4.

The stress response under elongation in the 2-2 direction and shear along the 1-3 direction are shown in Figure 8. The normalized root mean square deviation (NRMSD) is defined as,

$$\text{NRMSD} = \frac{\|\sigma - \sigma^{\text{ref}}\|_2}{\sqrt{N} \cdot \max\left(|\sigma^{\text{ref}}|\right)} = \frac{\sqrt{\frac{1}{N}\sum_{i=1}^{N}\left(\sigma_i - \sigma_i^{\text{ref}}\right)^2}}{\max\left(|\sigma^{\text{ref}}|\right)} \tag{26}$$

where N is the number of output intervals, σ_i is the simulation stress at the i-th output interval for a given RVE thickness, and σ_i^{ref} is the corresponding reference stress from the 10 μm model (Table 2).

Both 1 μm models underpredict the peak stress relative to the converged solution. Although the 1 μm reduced integration model exhibits a peak stress closer to the reference, its response is oscillatory and deviates considerably from the converged solution during the relaxation phase. The 1 μm full integration model is less oscillatory but underpredicts the peak stress to a greater extent. Despite these differences, the NRMSD values for both 1 μm models are similar ($\sim 6\%$), as the errors in the peak and relaxation phases partially offset each other. The 2 μm, 3 μm, and 10 μm reduced integration models converge to a common solution across both phases, indicating that the 2 μm RVE achieves a good balance between accuracy and computational efficiency.

2.6. Short-memory Principle

A key drawback of the fractional viscoelastic model is the need to store and retrieve the entire strain history in order to calculate the stress at the end of each increment. As a result, in an explicit time integration scheme, which

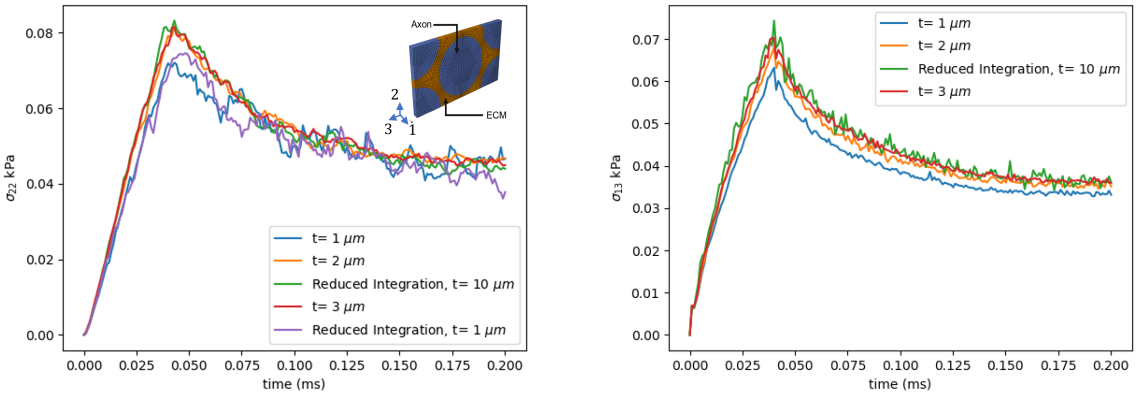

(a) (b)

Figure 8: (a) Comparison of stress along (a) transverse normal direction 2-2 (σ_{22}) (b) shear along direction 1-3 (σ_{13}), under a ramp-hold deformation with peak strain of 0.5% for different RVE thickness' and number of elements, applied to an RVE with vf = 0.4

typically requires small time increments, the number of computations can become prohibitively large. For large t, the role of the history of the strains near the lower terminal, i.e., near $t = 0$ can be neglected under certain assumptions. Podlubny [45] describes a method known as the "short-memory" principle which can be used to truncate the memory of strains required to compute the stress in eq. (20). Alotta et al. [44] also discuss examples of truncated memory for explicit simulations. While this reduces the cost of computation, it also comes at the price of decreased accuracy. The optimal memory length must be determined for each load profile based on the desired level of accuracy. We compute the reduced memory solution by essentially replacing the increasing number of terms in the summation in eq. (20) with a fixed value as the simulation progresses as shown below,

$$\frac{d^\beta f}{dt^\beta} = \left(\frac{1}{\Delta t}\right)^\beta \sum_{l=1}^{M+1} \varphi_l f\left((k+1-l)\,\Delta t\right) \tag{27a}$$

$$M = \min\{\frac{t}{\Delta t}, \frac{L}{\Delta t}\}, L = \gamma T, \gamma < 1 \tag{27b}$$

where L is the *Memory Length*, defined as a fraction of T, the total simulation time. During the early stages of the simulation ($t < L$), the number of terms in the summation is set to $k = \frac{t}{\Delta t}$ which increases with time. Once $t > L$, the terms in the summation is switched to "M" which is a fixed number of increments.

The application of the short-memory principle is demonstrated in Figure 9a using a unit cube model. The effect of truncating memory is evaluated by setting different fractions of the total simulation time as the memory length under a ramp-hold uniaxial extension with a maximum strain of 1%, where the ramp phase ends at 1 s and the strain is subsequently held constant (Figure 5a). For the ramp-hold strain, truncating the memory length up until the duration of the ramp phase reproduces the maximum stress in the model. The full and reduced kernels are identical until the current simulation time t exceeds L, after which error begins to accumulate as the simulation time grows larger. For memory lengths shorter than the ramp duration ($L < 1s$), the model overpredicts the peak stress. Motivated by this, we aim to compute the error bound due to memory truncation as a function of the maximum strain. Approximating this bound in terms of a maximum principle is reasonable for memory lengths exceeding the ramp phase, as the strain remains constant beyond this point. The error $e(t)$, for any time instant can be defined as,

$$e(t) = \begin{cases} 0, & t \leq L \\ -(\sigma(t) - \sigma_L(t)), & t > L \end{cases} \tag{28}$$

Formulating the error in this form ensures that $e(t)$ is a positive quantity as truncating memory leads to an overprediction of the stress. Using eq. (20), the error can be written as a function of the discarded terms in the sum as,

$$e(t) = -\left(K_\beta + \frac{4G_\beta}{3}\right)\frac{1}{\Delta t^\beta}\sum_{l=M+1}^{k+1}\phi_l \epsilon((k+1-l)\Delta t) \tag{29}$$

where $\varphi_l = (-1)^l \frac{\Gamma(\beta+1)}{\Gamma(\beta+1-l)l!}$. Using the property of the gamma function, $\Gamma(z-n) = (-1)^{n-1}\frac{\Gamma(-z)\Gamma(1+z)}{\Gamma(n+1-z)}, \forall n \in \mathbb{N}_0 \subset \mathbb{Z}$, we have

$$\phi_l = \frac{\Gamma(l-\beta)}{\Gamma(-\beta)l!} \tag{30}$$

and from the recurrence relation, $\Gamma(-\beta) = -\frac{\Gamma(1-\beta)}{\beta}$, ϕ_l can be written as,

$$\phi_l = \frac{-\beta\,\Gamma(l-\beta)}{\Gamma(1-\beta)\Gamma(l+1)} \tag{31}$$

For l sufficiently large such that $l-\beta \gg 1$, $\frac{\Gamma(l-\beta)}{\Gamma(l+1)}$ can be approximated as $l^{-(1+\beta)}$ using Stirling's formula. Substituting this form into eq. (30), e(t) can be written as,

$$e(t) = \left(K_\beta + \frac{4G_\beta}{3}\right)\frac{\epsilon_{max}}{\Delta t^\beta}\sum_{l=M+1}^{k+1}\frac{\beta}{\Gamma(1-\beta)}l^{-(1+\beta)} \tag{32}$$

Equation (32) can be approximated by an integral by rewriting the summation in the form of a Riemann sum, such that

$$e(t) = \left(K_\beta + \frac{4G_\beta}{3}\right)\frac{\beta\,\epsilon_{max}}{\Gamma(1-\beta)}\int_L^t x^{-(1+\beta)}dx \tag{33}$$

where $x = l\Delta t$ and $dx = \Delta t$. Thus, the error due to memory truncation at any time instant $t > L$ can be defined as,

$$e(t) = \left(K_\beta + \frac{4G_\beta}{3}\right)\frac{\beta\,\epsilon_{max}}{\Gamma(1-\beta)}(L^{-\beta} - t^{-\beta}) \tag{34}$$

An analytical expression for the root mean square error (RMSE) can be defined using eq. (34) as,

$$\text{RMSE}_{\text{analytical}} = \frac{1}{\sqrt{T}}\|e(t)\|_2 = \sqrt{\frac{1}{T}\int_L^T \left[C\left(L^{-\beta} - t^{-\beta}\right)\right]^2 dt} \tag{35}$$

where $\|e(t)\|_2 = \sqrt{\int_L^T [e(t)]^2\,dt}$ denotes the L^2 norm over the interval $[L, T]$. The final form of the equation is,

$$\text{RMSD}_{\text{analytical}} = C\Big(\frac{1}{T}\Big[L^{-2\beta}(T-L) - \frac{2L^{-\beta}(T^{1-\beta} - L^{1-\beta})}{1-\beta} + \frac{T^{1-2\beta} - L^{1-2\beta}}{1-2\beta}\Big]\Big)^{1/2} \tag{36}$$

where $C = \left(K_\beta + \frac{4}{3}G_\beta\right)\frac{\beta\epsilon_{\max}}{\Gamma(1-\beta)}$. The analytical RMSE from eq. (34) is compared with the RMSD computed from the numerical stress response for different memory lengths (Figure 9). The analytical RMSD forms an upper bound to the numerical error and converges to the numerical RMSD as the memory length increases. Furthermore, approximating the error using the maximum strain, even during the ramp phase, yields a reasonable estimate of the anticipated

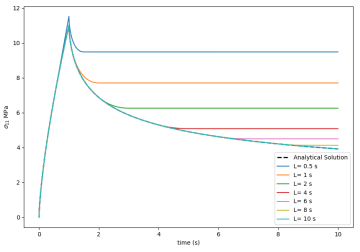

(a) A comparison of the tensile stress response of a unit cube under uniaxial extension between the exact solution and simulations with varying fractions of the total time as memory length, L.

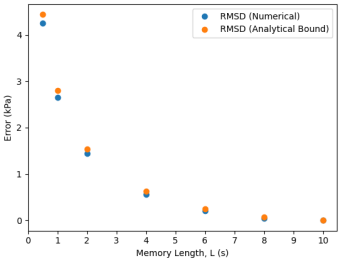

(b) A comparison of the analytical and numerical RMSD as a function of the memory length, L. The analytical RMSD forms an upper bound to the numerical error, converging toward it as L increases.

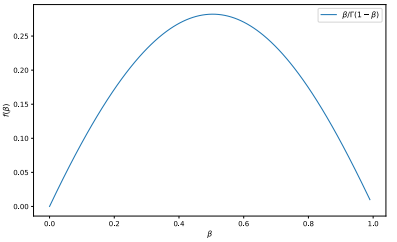

(c) Coefficient $f(\beta) = \frac{\beta}{\Gamma(1-\beta)}$ plotted over $\beta \in (0,1)$. The error-scaling factor vanishes at the integer-order limits and peaks at $\beta = 0.5$. The largest relative error are due to intermediate fractional orders.

Figure 9: An implementation of the "short-memory" principle for the unit cube example. Different fractions of the total simulation time are set as the memory length under a ramp-hold uniaxial extension with a maximum strain of 1% and a ramp duration of 9 s (Figure 5c). Truncating the memory length up until the duration of the ramp phase reproduces the maximum stress in the model. The full and reduced kernels are identical until the current simulation time t exceeds L, after which error begins to accumulate as the simulation time grows larger. The analytical RMSD forms an upper bound to the numerical error.

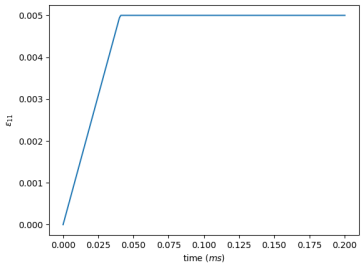

(a)

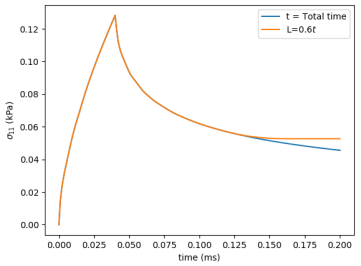

(b)

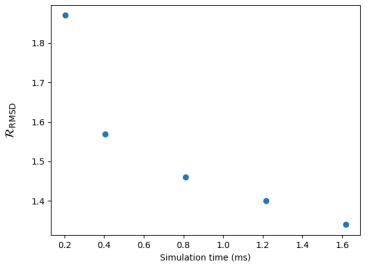

(c)

Figure 10: (a) Ramp-hold displacement loading profile for the bisphasic RVE with a peak strain of 0.5%. (b) A comparison of the tensile stress response along the fiber direction for an RVE with vf = 0.4, considering the full time history and a reduced-memory simulation with a memory length, L set to 60% of the total simulation time. (c) Convergence of the analytical RMSD bound toward the numerical RMSD with increasing simulation time T and $\frac{L}{T} = 0.6$. Here, $\mathcal{R}_{\text{RMSD}} = \text{RMSD}_{\text{analytical}}/\text{RMSD}_{\text{numerical}}$ is ratio of the analytical error to the numerical error. The decreasing ratio reflects the improved accuracy of the continuous integral approximation as the summand $l^{-(1+\beta)}$ varies continuously for larger l.

truncation error. Equation (36) suggests that the error due to memory truncation depends not only on L but also on the material constant C. This demonstrates that materials with larger generalized viscosity coefficients and intermediate fractional orders (Figure 9c) require a longer memory length than those with material parameters that lead to a smaller C, to achieve the same error tolerance.

We evaluate the effect of memory length on the stress response of a biphasic RVE with vf=0.4 using eq. (36) by setting $L = 0.6T$ under a ramp-hold displacement boundary condition (Figure 10b). For short simulation durations, approximating the discrete summation in eq. (32) by a continuous integral overestimates the error. For a duration $T = 0.2025$ ms (Figure 10a), the analytical error bound of 4.87×10^{-3} exceeds the numerical RMSD of 2.37×10^{-3} by a factor of 2. As the total simulation time increases, the analytical bound converges toward the numerical RMSD, with the ratio of analytical to numerical RMSD decreasing from 2 to 1.34 as T increases from 0.2025 ms to 1.620 ms (Figure 10c). This behavior reflects the fact that the summand $l^{-(1+\beta)}$ becomes increasingly continuous for larger l, reducing the discrepancy between the discrete sum and its continuous integral approximation. The decreasing ratio of

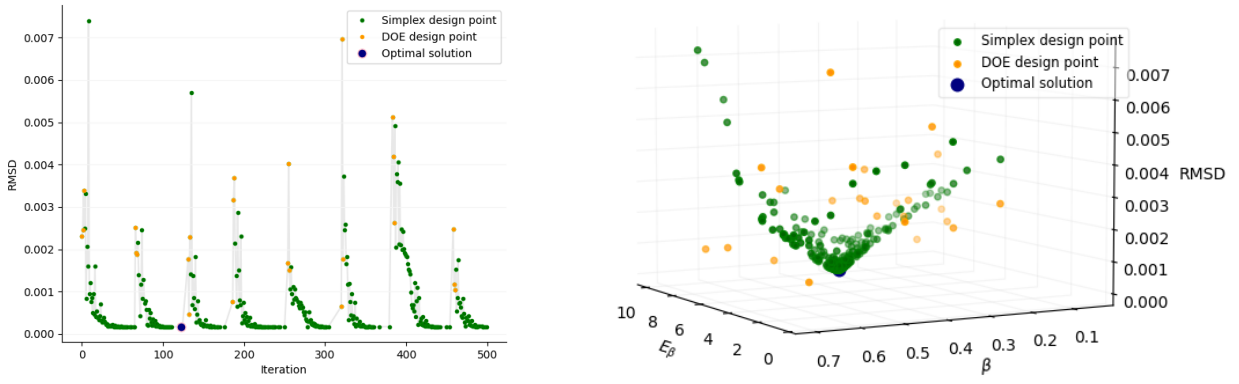

(a) (b)

Figure 11: Optimization plots for loading along the fiber direction (1-1), for an RVE with $VF = 0.4$. Orange points denote DOE-based reinitialization; green points denote Nelder-Mead simplex iterations and the blue point indicates the lowest RMSD achieved across all design points. (a) Objective function history plot showing the evolution of RMSD with iteration number. Multiple restarts with DOE sampling are performed to mitigate convergence to local minima. The Nelder-Mead simplex algorithm consistently converges to a minimum RMSD of $\mathcal{O}(10^{-4})$. (b) Optimization design landscape of RMSD vs E_β and β along the fiber direction. The landscape reveals an elongated valley with multiple parameter combinations yielding low RMSD values consistent with the ill-posed nature of the inverse problem under uniaxial loading.

analytical to numerical RMSD with increasing l serves as a diagnostic for identifying the simulation duration beyond which the material response is sufficiently relaxed. For an RVE with vf=0.4, containing 3904 hexahedral elements (C3D8) with full integration (8 integration points), a memory length of $L = 0.6T$ results in a deviation of 3.88% between the reduced-memory and full time-history simulations. The computing time on a single processor with 40 GB of RAM is reduced from 52 hours to 46 hours.

2.7. Optimization

An optimization-based calibration workflow is used to determine the homogenized fractional viscoelastic parameters for RVEs with varying volume fractions and along each loading direction. Nelder-Mead downhill simplex algorithm is used to determine the material parameters. Simplex is a geometric figure in $\mathbb{R}^n$ with $n + 1$ vertices in an n-dimensional space. It compares the values of the objective function at $N + 1$ vertices and gradually moves the polyhedron towards the optimal point by iteratively replacing the worst vertex with a point moved through the centroid of the remaining N points [55].

The workflow implemented using modeFRONTIER [56], computes the fractional viscoelastic stress for a set of input spring-pot parameters and minimizes the root mean square deviation (RMSD) between the computed stress and the homogenized stress from the FEM simulation. The optimization problem is formulated as shown in eq. (37), where J is the cost function, σ_{sim} is the FEM solution and σ_c is the computed stress.

$$\text{min} \qquad J = \sqrt{\frac{1}{m}\sum_{n=1}^{m}\frac{(\sigma_{sim} - \sigma_c)^2}{\sigma_{sim}^2}} \tag{37a}$$

$$\text{subject to} \qquad 0 \leq \beta \leq 1; \quad m > 0 \tag{37b}$$

A representative optimization plot is shown in Figure 11. For an optimization problem with 2 variables, the simplex polyhedron is a triangle. modeFRONTIER automatically initializes the simplex using DOE sampling. The evolutionary search strategy moves the initial points along with their function values, closer to the optimal point of the objective until the maximum number of iterations is reached or convergence is achieved. Multiple independent DOE restarts are performed to test convergence. In this study, a total of 500 iterations are used for each optimization problem. The self-initializing algorithm chooses 8 restarts with a total of 24 DOE sampling points ($\approx$ 5% of the total iterations).

The Nelder-Mead simplex algorithm consistently converges to a minimum RMSD of $\mathcal{O}(10^{-4})$. The design landscape reveals an elongated valley structure with multiple parameter combinations producing a similar stress response. The convergence of multiple independent restarts to the same valley floor confirms that this represents the global minimum region, with the ill-posedness being an intrinsic property of the inverse problem under uniaxial loading conditions.

3. Results

The homogenized fractional viscoelastic parameters, E_β, β, of the RVE, as a function of the volume fraction, evaluated under six loading directions, are illustrated in Figure 12 and Figure 13. E_β (spring-pot coefficient) with units $(\frac{kPa}{m s^\beta})$, is known as the generalized viscosity constant, representing both, the material's stiffness as well as its viscous behavior. The power-law exponent β serves as a bounding parameter in eq. (13) such that when $\beta = 0$, the model reduces to that of a spring with an elastic constant, whereas $\beta = 1$ produces the equation for a viscous dashpot. The two parameters taken together are used to compute the elastic modulus of the material.

The simulations indicate that the variation of the spring-pot coefficient, E_β, along the fiber direction is linear, whereas the variations along the other normal and shear directions are nonlinear. In the case of the fractional exponent β, its variation along the fiber direction follows a saturating exponential trend, approaching a plateau at high volume fractions. It can be observed that both E_β and β increase with higher axonal volume fractions. This trend aligns with existing data, which suggest that BWM glial cells are less viscous and significantly softer and more compliant than axons [57]. The linear variation of $E_{\beta_{11}}$ along the fiber direction is consistent with the rule-of-mixtures behavior observed in both strain rate–dependent [58] and strain rate–independent [59, 60] fiber composite materials. The saturating exponential behavior of β_{11} suggests that higher volume fractions lead to increased tissue viscosity.

The homogenized viscoelastic parameters for the loading directions [2-2, 3-3, 1-2, 1-3, 2-3] were fit to various functional forms, with the best fit achieved using a converging bi-logistic function. The curve fit was obtained by solving a nonlinear least squares problem using the Trust Region Reflective algorithm implemented in SciPy's optimization library. This algorithm iteratively solves trust-region subproblems, where the objective function is locally approximated using the Gauss-Newton method. The size of the trust region is governed by both the proximity to the parameter bounds and the gradient direction. This method is particularly well-suited for bounded curve fitting problems.

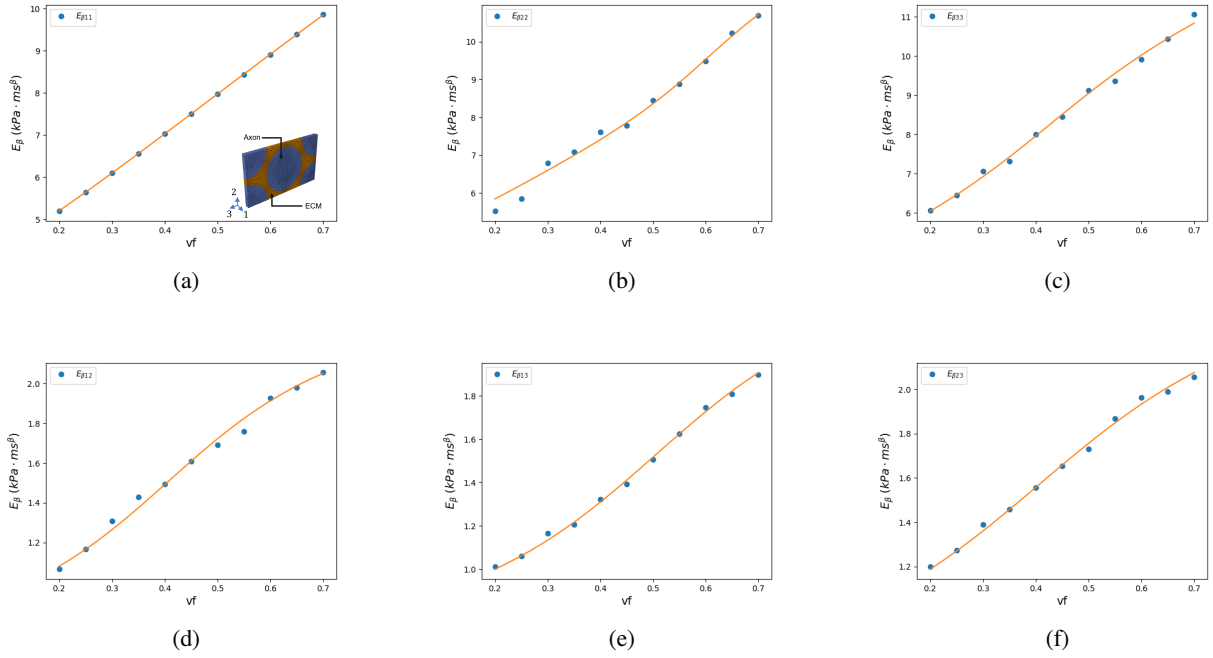

Figure 12: Homogenized fractional viscoelastic spring-pot coefficients (generalized viscosity constant) as a function of volume fraction under six loading directions. Subfigures (a)–(f) correspond to loading directions 1-1, 2-2, 3-3, 1-2, 1-3, and 2-3, respectively.

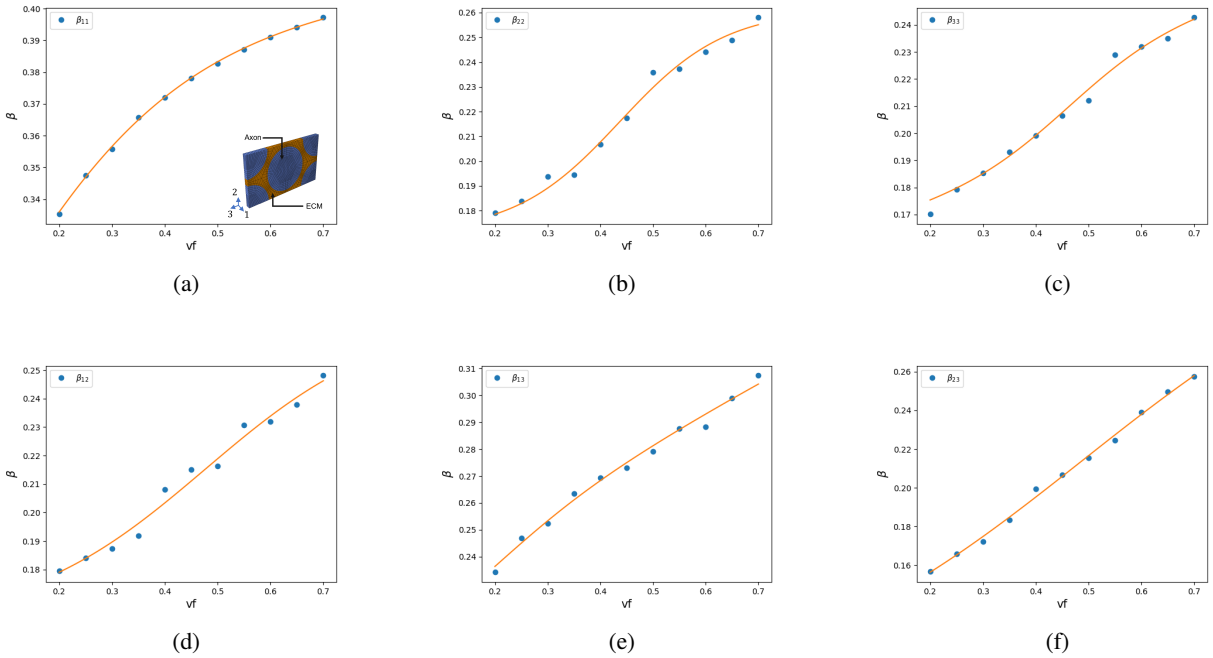

Figure 13: Homogenized fractional viscoelastic spring-pot exponent as a function of volume fraction under six loading directions. Subfigures (a)–(f) correspond to loading directions 1-1, 2-2, 3-3, 1-2, 1-3, and 2-3, respectively.

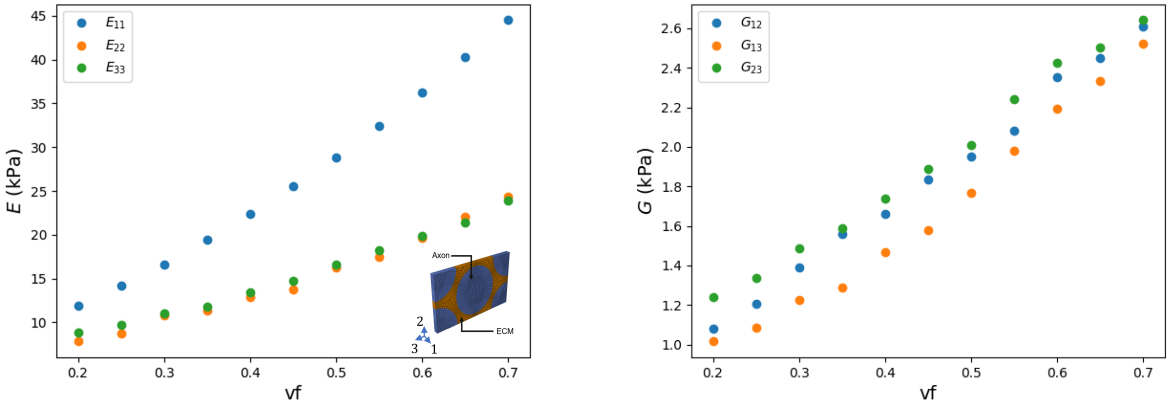

(a) Elastic modulus along normal directions: 1-1, 2-2, and 3-3. (b) Elastic modulus along shear directions: 1-2, 1-3, and 2-3.

Figure 14: Elastic moduli-like-parameters, with units kPa, under six loading directions obtained by combining the power-law parameters, E_β and β.

4. Discussion

Bi-logistic functions appear in the study of a wide range of biological systems [61]. The bi-logistic fit reveals two distinct transitions (inflection points) in material properties as axon volume fraction changes. For the CC with aligned fibers, the rate of change of the homogenized properties shows two stiffening stages: a lower rate when the axon volume fraction is low, followed by a higher rate when larger axon volume fraction stiffens the RVE. Thus, the RVE transitions from a glial matrix-driven to an axon-driven mechanical response. Sullivan et al., in their sensitivity analysis of the transverse shear viscoelastic properties of white matter tissue, observed a similar trend — where the effective moduli changed at a steeper rate for vf > 0.5 [16]. The spring-pot coefficients $E_{\beta_{22}}$ and $E_{\beta_{33}}$ deviate from the rule of mixtures towards Halpin-Tsai models as expected in fiber reinforced composites. Numerically, the RVE exhibits a slightly higher resistance to viscoelastic deformation along the horizontal axis ($E_{\beta_{33}}$) compared to the vertical axis ($E_{\beta_{22}}$). This anisotropy can be attributed to the hexagonal packing of the RVE, which provides a more direct, continuous load path in the 3-3 direction. Conversely, under shear, $E_{\beta_{12}}$ is greater than $E_{\beta_{13}}$ as the smaller fiber spacing along the 2-2 direction provides greater constraint against shear deformation in the 1-2 plane compared to the more compliant 1-3 response.

Given the units of E_β ($\frac{kPa}{ms^\beta}$), the spring-pot parameters can be more intuitively interpreted by combining them into a single shear-modulus-like parameter using the below equation [4],

$$E = (E_\beta * \eta^{-\beta})^{\frac{1}{1-\beta}}, \tag{38}$$

where E has the units of the shear modulus (kPa) and $\eta = 1.0\ kPa \cdot ms$ is the unit viscosity parameter [62]. Sack et al. report $\eta = 3.7 kPa \cdot ms$ derived from fitting a Zener model to multifrequency MRE data of the whole brain [4]. However, consistent region-specific values for η are not available. To avoid introducing an arbitrary region-specific assumption, $\eta = 1.0\ kPa \cdot ms$ is adopted as a reference value for computing the elastic modulus-like parameter in eq. (38). Another advantage of setting $\eta = 1.0\ kPa \cdot ms$ is that it allows the expression of the elastic modulus entirely in terms of the computed homogenized properties E_β and β. The elastic modulus along the three normal loading directions are shown in Figure 14a and the modulus along the three shearing directions are shown in Figure 14b. The results indicate that the variation of the elastic modulus with axon volume fraction is nonlinear in both the normal and shearing directions, and exhibits directional dependence—particularly in the CC, where axons are highly aligned and densely packed [63, 64]. This is particularly important in the context of neuropathological changes in different regions of the brain due to aging and disease. Multiple studies indicate that axon volume fraction does not remain constant with aging [5, 65]. It is therefore essential to quantify the effects of volume fraction on BWM stiffness, coupled with other factors such as myelin loss, axon degeneration, etc. to be able to make robust neuropathological assessments.

The model predicts that the average elastic modulus along the fiber direction (E_{11}) for the CC is 24.6 kPa which lies within the range of reported values for tensile modulus under small strain, high frequency loading [66]. The result is also in very good agreement with *in vitro* tensile characterization of brain tissue by Rashid et al. [67], which reported an elastic modulus in the range of 11–21 kPa for dynamic strain rates of $90/s$ for strain magnitudes of $0-0.1$. The model predictions are consistent with previous findings that brain tissue exhibits greater stiffness along the fiber direction than in the transverse direction [68]. This yields further support to the notion that axons are the primary contributors to the stiffness of the CC, despite the presence of other structural components such as blood vessels. While some studies report directional dependence of material properties in the CC [63, 64, 62], others have found no significant variation [69, 70]. The discrepancies among studies could stem from a range of additional factors, including differences in specimen type and size, temperature, experimental setup, and the nature of applied loading.

Along the shearing directions, the model predicts that the CC is stiffest under shear in the transverse direction (G_{23}), which is in agreement with existing experimental results [6, 63, 68]. The average shear modulus predicted by the model for the CC is 1.6 kPa to 2.1 kPa. Experimental shear moduli reported in the literature vary widely depending on species, tissue region, loading rate, and measurement technique, and the predicted values occupy the lower end of this distribution. For comparison, Rashid et al. [71] characterized porcine brain tissue under dynamic finite shear at a strain rate of 120 s^{-1}, close to the 123.5 s^{-1} used during the ramp phase in this study and reported an instantaneous shear modulus of 4.9 kPa (derived from a linear viscoelastic Prony series). Nicolle et al. [72] reported a shear modulus between 5 kPa and 10 kPa at sub-millisecond time scales under oscillatory shear using a high-frequency rheometer. These values are higher than the present predictions; however, this difference likely reflects variability in tissue region, sample preparation, and the specific viscosity parameter employed, and is consistent with the wide scatter observed across brain tissue mechanics literature. Furthermore, Liu et al. [52] demonstrated that a fractional viscoelastic model calibrated over a low-frequency range accurately predicted mechanical behavior up to 7.75kHz, supporting the use of a power-law framework across a broad frequency range. The characteristic frequency of $\approx$ 8.6 kHz (from the rise time relation $f_c \approx \frac{0.35}{t_{ramp}}$) considered in this study is comparable to the above validated range. Even at lower kHz frequencies, the data show a wide variation. Murphy et al. [73] observed a median stiffness of 25.0kPa at 1500 Hz in murine brains. In contrast, fitting the murine MRE data from Schregel et al. [74] to an equivalent power-law using eq. (38) yields 5.0 kPa at 1000 Hz, while data from Clayton et al. [26] yield 5.2 kPa at 1500 Hz and 14.6 kPa at 1800 Hz.

The average power-law exponent under shear predicted by the model for the CC is 0.2236–0.2531. Along the axial direction, the predicted average value of $\beta = 0.38$ is the highest among all directions, consistent with the conclusion of Kang et al. [28] that the power-law exponent is highest along the fiber direction. The power-law exponents reported in the literature for the whole brain span a wide range, from 0.265 [4, 14] to 0.339 [25], and up to 0.91 [75]. For BWM, reported power-law exponent values range from 0.337 [25] to 0.84 [75]. While most of these values were obtained via MRE characterization under low frequencies, the region-specific atlas compiled by Morrison et al. [75] reports an equivalent $\beta = 0.79$ for the CC. This value was synthesized by converting existing Prony-series coefficients—sourced from multiple studies across twelve brain regions and eight different mammals—into fractional-exponent attenuation power laws. In contrast, Ruhland et al. [76] report two power-law exponents from a high-frequency fractional Kelvin-Voigt model: a lower exponent ranging from 0.337 – 0.463 and a higher exponent between 0.933 – 0.961.

The significance of β is that it encodes information about the underlying tissue architecture. In this study, this becomes evident through the evolution of β as the volume fraction changes. This observation also offers a possible explanation for the variability of reported β values across different studies i.e., the magnitude of β varies based on the location and direction in which BWM is probed. A lower value of β (closer to 0) represents a structure that is more solid whereas $\beta \approx 1$ is more representative of a fluid-like material dominated by viscous dissipation. From a rheological standpoint, the arrangement of springs and dashpots, representing distinct elastic and viscous effects can be tuned such that the overall response of the model reduces to the form in eq. (16). Thus, the emergent parameter β encapsulates the complex interplay between the different microstructural elements.

4.1. Efficient Computing

Given the computational expense of the GL operator, which requires storing and retrieving strain histories, we explore additional strategies to improve the computational efficiency of its implementation. For an explicit time integration scheme, in addition to the short-memory principle discussed in Section 2.5, increasing the time step size can improve the computing speed. However, the stable time increment depends on the dilatational wave speed of the material and the smallest element length. The above geometric and material constraints limit the size of the "stability limit". Exceeding the stable time increment could result in numerical instability that may lead to unbounded solutions.

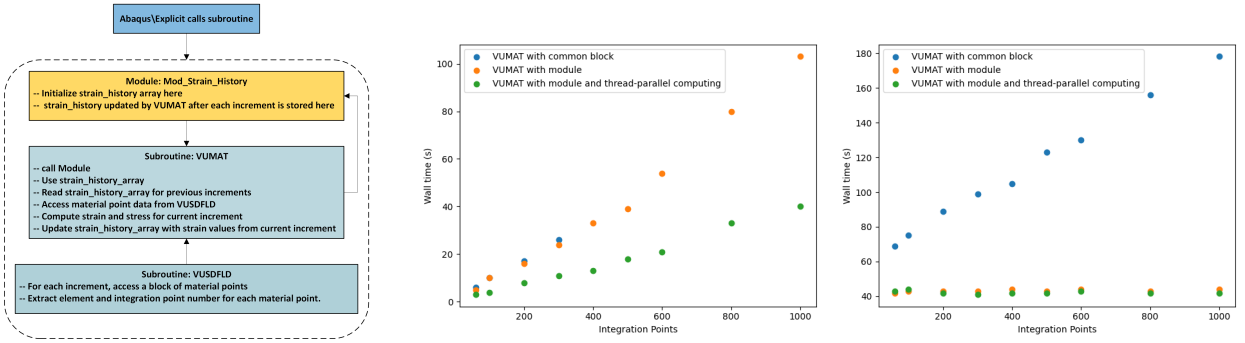

(a) (b) (c)

Figure 15: (a) A representation of the algorithmic workflow for the `VUMAT`. The `VUSDFLD` subroutine tracks the material points at the start of each increment [44]. The array that contains the strain history is defined and stored inside a module. The `VUMAT` subroutine calls `VUSDFLD`, the strain history array from the module, updates the strain history at the end of each increment for each element and integration point. The updated array is stored in the module. Runtime performance comparison between common-block, module-based, and thread-parallel `VUMAT` implementations: (b) on a Windows machine with 16 GB RAM and 4 cores, and (c) on a single node of a Linux HPC with 120 GB RAM and 4 cores.

With automatic solver-based time incrementation, even conservative estimates of the stable time increment can be increased as the simulation progresses and the element lengths change on account of the deformation. But simulations that require storing and retrieving field variables requires a fixed stable time increment which is computationally expensive.

Models with stored field variable histories implemented through user subroutines in Abaqus typically rely on `COMMON` blocks which define an area of memory accessible globally by all functions and subroutines in the code [44, 77, 78, 79]. This, however, poses two major challenges, especially during parallel execution. First, the definition of common blocks can vary between functions and subroutines which could lead to subtle errors with no obvious cause. Second, given the global scope of the common block, mutexes are essential to ensure thread safety during thread-based parallel execution. This, however, degrades performance.

A possible workaround to these challenges is to implement a Fortran 90–based `MODULE` for storing strain histories. Modern Fortran compilers including Intel and GNU support mixed F77-F90 codebases. Fortran modules enable explicit control over variable/array scope and promote modular code architecture. Furthermore, imports (`USE`) and exports (`PUBLIC`) are explicitly defined, which limits the scope of the strain history array to the module and the `VUMAT`, rather than being re-imported into every procedure or interface scope. Here we show that incorporating these methods result in thread-safe parallel code that yields significant time savings.

In this study, we replace the common block methodology with a Fortran module that stores the strain histories (see 15a). The `VUMAT` subroutine calls another subroutine, `VUSDFLD`, which tracks the element number and integration point. The strain history array is then accessed by the `VUMAT` for retrieving the strains and computing the updated strain, which is stored back in the module. The module controls the visibility and access to the strain history array, thereby ensuring a more robust, thread-safe behavior during parallel execution.

The efficiency of a modular implementation of the `VUMAT` subroutine is demonstrated using a 1D beam example developed by Alotta et al [44]. The original example consists of a bar modeled with ten 1D linear truss elements, with its left end constrained and a $10N$ force applied at the right end, held constant for $t = 5s$. We evaluate the performance of the subroutine by incrementally increasing the number of elements in the model and measuring the computation time. Since the strain history array must be allocated at the start of the subroutine, implementing it via common blocks results in large data structures being placed on the runtime stack, which can quickly exceed the stack size limit, causing execution failure. For the test case, with common blocks, on a Windows machine with four cores and 16 GB RAM, the stack size limit was exceeded with 300 elements (see Figure 15b). On a linux high-performance cluster (HPC) that supports large data structures, using a module for the strain history in the `VUMAT` is significantly more efficient than using common blocks as the model size increases (see Figure 15c).

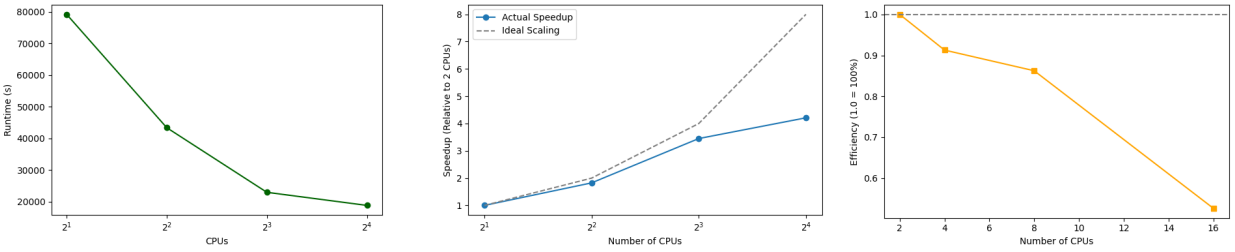

(a) (b) (c)

Figure 16: (a) Wall-clock runtime (s) vs. number of CPU cores; (b) observed speedup $S_p = T_2/T_p$, where T_2 denotes the runtime for $p = 2$; and (c) parallel efficiency $E_p = S_p/(p/2)$. Results are benchmarked against a baseline of $p = 2$ processors, exhibiting good parallel scaling through $p = 8$ with an observed performance decay at $p = 16$ due to reduced load balancing.

The performance of the two cases is compared against a thread-parallel execution of the `VUMAT` using the strain history module (see 15a). On the Windows machine with 4 cores, the performance gain is visible even for small models such as the 1D bar example. On a Linux machine using 4 cores, the performance for the `VUMAT` with the module is similar between serial and parallel execution. This is likely because, for a small model running on a large HPC, the serial code is already operating near its optimal capacity. Performance gains can be observed as the model size increases. For large 3D problems, computational throughput can be optimized by identifying the ideal degree of shared-memory parallelism for a given model size. This prevents performance degradation due to improper load balancing and an increased overhead of managing additional threads. To characterize this behavior, the runtime performance for the plate-with-a-hole benchmark was evaluated under strong scaling analysis using domain-level decomposition. Parallel execution on $p = 2$ cores on a node with 120 GB RAM is set as the reference baseline. For a discretization consisting of 8,720 reduced-integration hexahedral elements, the results demonstrate good parallel scaling up to 8 cores. However, at $p = 16$, the parallel efficiency diminishes to approximately 50%. This performance plateau suggests that for this specific model size, the computational workload per subdomain (545 elements per core) is no longer sufficient to offset the inherent overhead of thread management as the element-to-processor ratio decreases.

For the RVE with vf=0.4, the initial simulation time of 52 hours was reduced to 27 hours through the implementation of truncated memory and thread-based parallelization (leveraging 16 cores and 80 GB RAM). By further increasing the stable time increment and employing reduced-integration elements, the total runtime was further reduced to 5.15 hours. While reduced integration achieves exceptional speedup, care is required when handling more complex models such as triphasic systems; here, the presence of two stiffer regions (axon and myelin) surrounded by a much softer region (glia) may lead to significant chattering in the homogenized stress. Addressing this often necessitates a much finer mesh and a thicker RVE to mitigate numerical noise, essentially negating the computational speedup due to the increased element count. That said, for the biphasic RVE, this represents an order-of-magnitude improvement in computational performance compared to the baseline implementation.

4.2. Limitations

This study has a number of limitations. First, since BWM tissue exhibits dependence on both magnitude and rate of strain, the variation of homogenized properties with volume fraction obtained under small strain, high strain-rate loading conditions may differ substantially under other loading profiles. The material models for the biphasic RVE are calibrated using data from low-frequency oscillatory shear experiments, and the constituent parameters should be interpreted as effective values within the fractional framework. To the best of our knowledge, the viscoelastic properties of axons and ECM are not characterized at high strain rates. The extension of the power-law model to the high strain rate regime is motivated by experimental evidence demonstrating power-law viscoelastic behavior in brain tissue over a wide range of frequencies [4, 26, 76, 52]. Unlike Prony series models, which are associated with discrete relaxation times and are therefore tuned to specific experimental frequency windows, the power-law model describes a continuous distribution of relaxat1ion processes, making it naturally suited for application across a broad frequency range. While the homogenized properties along the fiber direction are consistent with reported values from high strain rate experiments on white matter tissue, the predicted shear moduli are comparatively lower than reported values. The

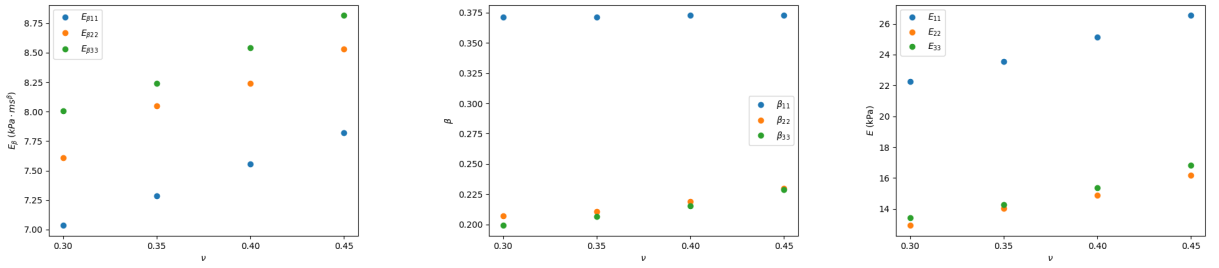

(a) (b) (c)

Figure 17: Homogenized fractional viscoelastic spring-pot parameters as a function of ν under normal loading directions. (a) generalized viscosity constant, E_β. (b) Spring-pot exponent, β (c) Elastic modulus-like parameter (kPa) obtained by combining E_β and β via eq. (38).

biphasic idealization of the RVE and the value of the viscosity parameter η may contribute to this discrepancy. An additional contributing factor is that the model may underestimate the material's attenuation behavior in the high-frequency domain, where the loss modulus is known to dominate over the storage modulus in whole brain and white matter tissue [75]. Accurately capturing this behavior over a broad frequency range may require additional experimental data at high frequencies and potentially a more complex fractional constitutive model beyond the springpot [76].

Second, the homogenized fractional viscoelastic properties are reported for a Poisson's ratio of $\nu = 0.3$ for both the axon and the glial matrix. While brain tissue is generally considered nearly incompressible with Poisson's ratios typically reported between 0.45 and 0.499, values as low as 0.33 have been reported in prior experimental and computational studies of axon mechanics [50, 51]. This places the present model firmly in the compressible regime. A parametric study of the sensitivity of the homogenized fractional viscoelastic parameters to the choice of Poisson's ratio is presented in Figure 17, for an RVE with vf = 0.4, with ν varied from 0.3 to 0.45. The results indicate a monotonic increase in E_β with Poisson's ratio across all normal loading directions. The fractional exponent β remains essentially unchanged across the entire range of ν for all loading directions, consistent with its interpretation as an intrinsic measure of the underlying tissue architecture that is governed primarily by the fiber-matrix geometry. Under pure shear loading, the homogenized parameters are insensitive to ν, consistent with the theoretical expectation that the volumetric response does not contribute to shear stress in a periodic biphasic RVE with identical Poisson's ratios in both phases. This decoupling suggests that, within the present modeling framework, uniaxial and pure shear tests alone are insufficient to effectively characterize the mechanical properties of white matter tissue. That said, the primary contributions of this study, i.e., the fractional viscoelastic framework, the thread-safe `VUMAT` implementation, and the qualitative trends in homogenized parameters with volume fraction and loading direction are expected to be robust. Simulations across the full range of volume fractions and loading directions with $\nu = 0.45$ are currently underway and will be reported in a follow-up study.

Third, the model assumes a biphasic periodic RVE with uniformly distributed and perfectly aligned axons in an ECM. While some regions of BWM containing highly aligned, densely distributed axons can be approximated by such models, and such representations have been used in prior studies [16, 18, 50], they remain strictly idealized. In reality, even in regions such as the CC, axonal dispersion, waviness, and fiber crossings deviate markedly from this idealized representation. Furthermore, the impact of myelin which plays a vital role in regulating the mechanical response in BWM is not considered in this model. These factors highlight the need to move toward micromechanical models that account for architectural organization, i.e., clustering/random versus uniform distributions, presence of vascular structures, cellular tracts, etc [63].

Fourth, the viscosity parameter used in this study is $\eta = 1.0\, kPa \cdot ms$, adopted as a unit reference value in the absence of consistent region-specific data for the corpus callosum. We acknowledge that accounting for a more physically representative value of η would shift the predicted elastic moduli. Furthermore, because the extraction of homogenized properties is based on uniaxial tests derived from sparse material data, the resulting optimization problem is inherently unconstrained and ill-posed. Consequently, multiple combinations of E_β and β can yield nearly identical homogenized stress responses. While the low dimensionality of the parameter space and the use of a design-of-experiments-based initialization mitigates the risk of convergence to local minima, the lack of multiaxial experimental

data remains a fundamental concern. This underscores the need for richer datasets with multiple loading scenarios, which would allow for physically motivated constraints in the optimization problem and improve the uniqueness of the identified parameters.

Finally, the fractional viscoelastic model provides a concise physical description of the observed power-law rheology of BWM compared to Prony series models. However, its implementation through the GL operator scheme is computationally expensive. Storing and retrieving field variable histories requires preallocating large amounts of memory, making the GL operator significantly more computationally expensive than Prony series models. This highlights the need to investigate the effects of further truncating the memory using circular binning for different loading regimes. Moving forward, investigations focusing on the implementation of faster algorithms, such as quadrature based solutions to Abel integral formulation for solving the RL fractional integral or sum of exponents approximations [80] are essential.

5. Conclusions

To the best of our knowledge, this exploratory study is the first of its kind to propose and implement a 3D fractional viscoelastic finite element model of the corpus callosum of BWM in the time domain. Several soft tissues including BWM exhibit power-law responses under oscillatory shear tests such as MRE. In this study, drawing on the principle of scale invariance prominently expressed in the brain, we posit that the power-law behavior observed at the tissue level extends across length scales to the microstructural realm of the axons. This hypothesis has indeed formed the basis of multifrequency MRE [23], but its application to cellular structures does not consider the microstructural architecture and material anisotropy.

It is often difficult to physically interpret the material response of such structures even in the linear limit of small deformations within the classical framework of springs and dashpots — which give rise to Maxwell-Debye exponential based Prony series. While the Prony series is readily implemented and widely available in commercial finite element software, it remains a strictly empirical representation that, at best, captures only a snapshot of the underlying dynamical processes. There are additional challenges; for example, even a seemingly simple two-parameter Prony series model requires the estimation of five material constants, and when incorporated into multiscale, multiphase models, the number of parameters can increase substantially. In this context, the language of fractional calculus, through the construct of a spring-pot provides a succinct ontological framework well-suited for modeling and quantifying the power-law behavior observed in BWM.

The mechanical response of the homogenized tissue can be characterized by two parameters, namely a generalized viscosity constant, E_β, and a power-law exponent, β. E_β represents the material's stiffness as well as its viscous behavior. β serves as a bounding parameter which encodes information about the underlying tissue architecture. Using complex shear moduli data from oscillatory shear tests on porcine white matter tissue, a power-law model describing the material constants for the axons and ECM is developed. The fractional viscoelastic model is numerically implemented using the GL operator in a Fortran `VUMAT` subroutine and validated with benchmark examples. The biphasic finite element model of hexagonally packed axons in an ECM is developed in Abaqus FEA with periodic boundary conditions and a ramp-hold displacement-controlled boundary condition. An explicit time integration scheme is used to compute the evolution of stress in the model along six loading directions for varying volume fractions of axons in an ECM. An optimization algorithm is then used to solve the inverse problem of extracting the homogenized properties for the biphasic model.

The model predicts that both E_β and β increase with higher axonal volume fractions indicating that glial cells are less viscous, significantly softer and more compliant than the axons. We also observe that the variation of E_β with volume fraction, along the fiber direction is linear, whereas the variation along the transverse normal and shear directions are nonlinear. With β, the variation is nonlinear along all the loading directions with a saturating exponential behavior along the fiber direction. This indicates that β increases rapidly at low volume fractions before saturating at high volume fractions signaling greater composite viscosity at higher axonal content. For off-fiber directions, the variation of both E_β and β is best approximated by a bi-logistic function with two stiffening stages: a lower, glial matrix-driven rate when the axon volume fraction is low, followed by a higher rate once larger axonal content reinforces the RVE. The magnitude of E_β determines the solid-fluid behavior [4]. The fractional viscoelastic model not only reinforces this interpretation but also sheds further light on the nature of its variation and directional dependence. By combining the fractional viscoelastic constants into a single shear-modulus-like parameter along each loading direction, we observe that the variation of elastic moduli with volume fraction along all loading directions is nonlinear.

This nonlinearity is particularly important in the context of region-specific properties and neuropathological changes due to aging and disease. The model is well-suited for describing regions of BWM with aligned axonal fibers such as the CC. The predicted elastic modulus along the fiber direction is in good agreement with experimental observations, while the predicted shear moduli are comparatively lower than reported values.

In this study we also demonstrate an efficient, thread-safe implementation of the GL operator, which requires storing and retrieving of the strain history for computing the evolution of stress. The implementation leverages modern Fortran language based modules that enable explicit control over variable/array scope and promote modular code architecture. The performance gain in using a `Module`-based subroutine over traditional implementations with `COMMON` blocks is demonstrated through 1D and 3D examples on both, windows and linux computing platforms. We observe that the proposed methodology is significantly more efficient than existing approaches. Furthermore, by incorporating shared-memory parallelism, we achieve a speedup of ≈ 3.5 between 2 and 8 CPU cores demonstrating a high efficiency of 86%. We also derive a closed form expression for the analytical RMSD which forms a conservative upper bound to the numerical error and converges to the numerical RMSD as the memory length increases. The error estimate demonstrates that materials with a larger material constant, C require a longer memory length than those with smaller C to achieve the same error tolerance. The ratio of analytical to numerical RMSD serves as a diagnostic for identifying the simulation duration beyond which the material response is sufficiently relaxed. Overall, we demonstrate up to a 50% reduction in runtimes for the simulations of the BWM RVEs by incorporating modular array access, the short-memory principle and thread-parallel execution. By further incorporating volume fraction-specific stable time increments and employing reduced-integration elements where appropriate, an order-of-magnitude improvement in computational performance compared to the baseline implementation can be achieved.

Ethics statement

The authors confirm that all procedures described in the paper were performed in compliance with relevant laws and institutional guidelines and have been approved by the appropriate institutional committee(s).

Declaration of Competing Interest

The authors declare the following financial interests/personal relationships which may be considered as potential competing interests:

Assimina A Pelegri reports financial support was provided by the National Science Foundation. John G Georgiadis reports financial support from the R.A. Pritzker endowed chair. Parameshwaran Pasupathy has no known competing financial interests or personal relationships that could have appeared to influence the work reported in this paper.

Acknowledgments

The authors gratefully acknowledge the support provided by NSF via CMMI-1436743, CMMI-1762774 grants and by the R.A. Pritzker endowed chair. The authors also gratefully acknowledge Baoxiang Shan, PhD., for insightful discussions on the development of Fortran subroutines. In addition, the authors also thank Stephen S. Recchia, Ph.D., and Adrian Blot for their valuable insights on debugging and improving code performance. Finally, the authors thank Nader Fateh of ESTECO North America for generously granting a research modeFRONTIER license.

References

[1] D. N. Bullock, E. A. Hayday, M. D. Grier, W. Tang, F. Pestilli, S. R. Heilbronner, A taxonomy of the brain's white matter: twenty-one major tracts for the 21st century, Cerebral Cortex 32 (2022) 4524–4548.

[2] S. Chatelin, A. Constantinesco, R. Willinger, Fifty years of brain tissue mechanical testing: From in vitro to in vivo investigations, Biorheology 47 (2010) 255–276.

[3] Y.-J. Jeon, S.-E. Park, H.-M. Baek, Predicting brain age and gender from brain volume data using variational quantum circuits, Brain Sciences 14 (2024).

[4] I. Sack, B. Beierbach, J. Wuerfel, D. Klatt, U. Hamhaber, S. Papazoglou, P. Martus, J. Braun, The impact of aging and gender on brain viscoelasticity, Neuroimage 46 (2009) 652–657. Publisher: Elsevier.

[5] A. Z. Burzynska, C. Anderson, D. B. Arciniegas, V. Calhoun, I.-Y. Choi, A. Mendez Colmenares, A. F. Kramer, K. Li, J. Lee, P. Lee, M. L. Thomas, Correlates of axonal content in healthy adult span: Age, sex, myelin, and metabolic health, Cerebral Circulation - Cognition and Behavior 6 (2024) 100203.

[6] K. B. Arbogast, S. S. Margulies, Material characterization of the brainstem from oscillatory shear tests, Journal of biomechanics 31 (1998) 801–807.
[7] R. L. Saiki, Current and evolving management of traumatic brain injury, Critical Care Nursing Clinics of North America 21 (2009) 549–559. Neuroscience.
[8] Y. Suzuki, M. Hori, K. Kamiya, I. Fukunaga, S. Aoki, M. Van Cauteren, Estimation of the Mean Axon Diameter and Intra-axonal Space Volume Fraction of the Human Corpus Callosum: Diffusion q-space Imaging with Low q-values, MRMS 15 (2016) 83–93.
[9] Q. Fan, Q. Tian, N. A. Ohringer, A. Nummenmaa, T. Witzel, S. M. Tobyne, E. C. Klawiter, C. Mekkaoui, B. R. Rosen, L. L. Wald, D. H. Salat, S. Y. Huang, Age-related alterations in axonal microstructure in the corpus callosum measured by high-gradient diffusion MRI, NeuroImage 191 (2019) 325–336.
[10] M. Eilbes, Neuroanatomical planes in human brains, https://app.biorender.com/biorender-templates/details/t-652895179300787 3fb7fa81a-neuroanatomical-planes-in-human-brains, 2025. Accessed: 2025-08-08.
[11] T. J. Edwards, R. J. Dean, G. A. Robinson, J. Knight, S. A. Mandelstam, L. J. Richards, Microstructural analysis does not support altered interhemispheric wiring of the human anterior commissure in corpus callosum dysgenesis, NeuroImage: Clinical 44 (2024) 103692.
[12] S. Y. Huang, Q. Tian, Q. Fan, T. Witzel, B. Wichtmann, J. A. McNab, J. Daniel Bireley, N. Machado, E. C. Klawiter, C. Mekkaoui, L. L. Wald, A. Nummenmaa, High-gradient diffusion MRI reveals distinct estimates of axon diameter index within different white matter tracts in the in vivo human brain, Brain Struct Funct 225 (2020) 1277–1291.
[13] C. L. Johnson, M. D. McGarry, A. A. Gharibans, J. B. Weaver, K. D. Paulsen, H. Wang, W. C. Olivero, B. P. Sutton, J. G. Georgiadis, Local mechanical properties of white matter structures in the human brain, NeuroImage 79 (2013) 145–152.
[14] J. Wuerfel, F. Paul, B. Beierbach, U. Hamhaber, D. Klatt, S. Papazoglou, F. Zipp, P. Martus, J. Braun, I. Sack, Mr-elastography reveals degradation of tissue integrity in multiple sclerosis, NeuroImage 49 (2010) 2520–2525.
[15] C. Kiss, S. Wurth, B. Heschl, M. Khalil, T. Gattringer, C. Enzinger, S. Ropele, Low-frequency MR elastography reveals altered deep gray matter viscoelasticity in multiple sclerosis, NeuroImage: Clinical 42 (2024) 103606.
[16] D. J. Sullivan, X. Wu, N. R. Gallo, N. M. Naughton, J. G. Georgiadis, A. A. Pelegri, Sensitivity analysis of effective transverse shear viscoelastic and diffusional properties of myelinated white matter, Physics in Medicine and Biology 66 (2021) 3.
[17] A. Montanino, S. Kleiven, Utilizing a structural mechanics approach to assess the primary effects of injury loads onto the axon and its components, Frontiers in neurology (2018) 643.
[18] S. Javid, A. Rezaei, G. Karami, A micromechanical procedure for viscoelastic characterization of the axons and ecm of the brainstem, Journal of the Mechanical Behavior of Biomedical Materials 30 (2014) 290–299.
[19] N. Reiter, A. Schäfer, S. Auer, F. Paulsen, S. Budday, Modeling the finite viscoelasticity of human brain tissue based on microstructural information, Proc Appl Math and Mech 23 (2023) e202300234.
[20] W. Li, D. E. T. Shepherd, D. M. Espino, Investigation of the Compressive Viscoelastic Properties of Brain Tissue Under Time and Frequency Dependent Loading Conditions, Ann Biomed Eng 49 (2021) 3737–3747.
[21] C. Lai, Y. Chen, T. Wang, J. Liu, Q. Wang, Y. Du, Y. Feng, A machine learning approach for magnetic resonance image–based mouse brain modeling and fast computation in controlled cortical impact, Med Biol Eng Comput 58 (2020) 2835–2844.
[22] X. Wu, P. Pasupathy, A. A. Pelegri, On the application of hybrid deep 3D convolutional neural network algorithms for predicting the micromechanics of brain white matter, Computer Methods and Programs in Biomedicine 256 (2024) 108381.
[23] I. Sack, K. Jöhrens, J. Würfel, J. Braun, Structure-sensitive elastography: on the viscoelastic powerlaw behavior of in vivo human tissue in health and disease, Soft matter 9 (2013) 5672–5680.
[24] A. Fehlner, J. R. Behrens, K. Streitberger, S. Papazoglou, J. Braun, J. Bellmann-Strobl, K. Ruprecht, F. Paul, J. Würfel, I. Sack, Higher-resolution MR elastography reveals early mechanical signatures of neuroinflammation in patients with clinically isolated syndrome, Magnetic Resonance Imaging 44 (2016) 51–58.
[25] M. Kurt, L. Wu, K. Laksari, E. Ozkaya, Z. M. Suar, H. Lv, K. Epperson, K. Epperson, A. M. Sawyer, D. Camarillo, et al., Optimization of a multifrequency magnetic resonance elastography protocol for the human brain, Journal of Neuroimaging 29 (2019) 440–446.
[26] E. H. Clayton, J. R. Garbow, P. V. Bayly, Frequency-dependent viscoelastic parameters of mouse brain tissue estimated by MR elastography, Phys. Med. Biol. 56 (2011) 2391–2406.
[27] E. Nicolas, S. Calle, S. Nicolle, D. Mitton, J.-P. Remenieras, Biomechanical characterization of ex vivo human brain using ultrasound shear wave spectroscopy, Ultrasonics 84 (2018) 119–125.
[28] W. Kang, L. Wang, Y. Fan, Viscoelastic response of gray matter and white matter brain tissues under creep and relaxation, Journal of Biomechanics 162 (2024) 111888.
[29] A. Mishra, R. O. Cleveland, Rheological properties of porcine organs: measurements and fractional viscoelastic model, Front. Bioeng. Biotechnol. 12 (2024) 1386955.
[30] G. F. Grosu, A. V. Hopp, V. V. Moca, H. Bârzan, A. Ciuparu, M. Ercsey-Ravasz, M. Winkel, H. Linde, R. C. Mureșan, The fractal brain: scale-invariance in structure and dynamics, Cerebral Cortex 33 (2023) 4574–4605.
[31] P. Pasupathy, J. G. Georgiadis, A. A. Pelegri, A fractional viscoelastic model of the axon in brain white matter, Belgrade, Serbia, p. 070002.
[32] K. B. Arbogast, S. S. Margulies, A fiber-reinforced composite model of the viscoelastic behavior of the brainstem in shear, Journal of Biomechanics 32 (1999) 865–870. Publisher: Elsevier BV.
[33] A. Rohatgi, Webplotdigitizer, ????
[34] J. E. Caffyn, G. W. S. Blair, Significance of Power-Law Relations in Rheology, Nature 155 (1945) 171–172.
[35] G. Scott Blair, The role of psychophysics in rheology, Journal of Colloid Science 2 (1947) 21–32.
[36] Survey of Applications of the Fractional Calculus, in: Mathematics in Science and Engineering, volume 198, Elsevier, 1999, pp. 261–307.
[37] K. Adolfsson, M. Enelund, P. Olsson, On the fractional order model of viscoelasticity, Mechanics of Time-dependent materials 9 (2005) 15–34.
[38] A. I. Fedorchenko, INTRODUCTION TO FRACTIONAL CALCULUS, 2008.

[39] R. L. Bagley, P. J. Torvik, A Theoretical Basis for the Application of Fractional Calculus to Viscoelasticity, Journal of Rheology 27 (1983) 201–210.
[40] A. Bonfanti, J. L. Kaplan, G. Charras, A. Kabla, Fractional viscoelastic models for power-law materials, Soft Matter 16 (2020) 6002–6020.
[41] G. Alotta, O. Barrera, A. C. Cocks, M. D. Paola, On the behavior of a three-dimensional fractional viscoelastic constitutive model, Meccanica 52 (2017) 2127–2142.
[42] Chapter 2 - fractional derivatives and integrals, in: I. Podlubny (Ed.), Fractional Differential Equations, volume 198 of *Mathematics in Science and Engineering*, Elsevier, 1999, pp. 41–119.
[43] A. Schmidt, L. Gaul, Finite element formulation of viscoelastic constitutive equations using fractional time derivatives, Nonlinear Dynamics 29 (2002) 37–55.
[44] G. Alotta, O. Barrera, A. Cocks, M. Di Paola, The finite element implementation of 3d fractional viscoelastic constitutive models, Finite Elements in Analysis and Design 146 (2018) 28–41.
[45] Chapter 7 - numerical evaluation of fractional derivatives, in: I. Podlubny (Ed.), Fractional Differential Equations, volume 198 of *Mathematics in Science and Engineering*, Elsevier, 1999, pp. 199–221.
[46] W. Tian, L. Qi, X. Chao, J. Liang, M. Fu, Periodic boundary condition and its numerical implementation algorithm for the evaluation of effective mechanical properties of the composites with complicated micro-structures, Composites Part B: Engineering 162 (2019) 1–10.
[47] S. Sádaba, M. Herráez, F. Naya, C. González, J. Llorca, C. Lopes, Special-purpose elements to impose Periodic Boundary Conditions for multiscale computational homogenization of composite materials with the explicit Finite Element Method, Composite Structures 208 (2019) 434–441.
[48] M. Smith, ABAQUS/Standard User's Manual, Version 2020, Dassault Systèmes Simulia Corp, United States, 2020.
[49] S. L. Omairey, P. D. Dunning, S. Sriramula, Development of an abaqus plugin tool for periodic rve homogenisation, Engineering with Computers 35 (2019) 567–577.
[50] F. Hasan, K. A. Mahmud, M. I. Khan, A. Adnan, Viscoelastic damage evaluation of the axon, Front. Bioeng. Biotechnol. 10 (2022) 904818.
[51] R. Wang, M. Sarntinoranont, Biphasic analysis of rat brain slices under creep indentation shows nonlinear tension-compression behavior, Journal of the Mechanical Behavior of Biomedical Materials 89 (2019) 1–8.
[52] Y. Liu, T. K. Yasar, T. J. Royston, Ultra wideband (0.5–16 kHz) MR elastography for robust shear viscoelasticity model identification, Phys. Med. Biol. 59 (2014) 7717–7734.
[53] A. Schellenberger, M. Jenderka, T. Drießle, M. Ledwig, I. Sack, A compact 0.5 T MR elastography device and its application for studying viscoelasticity changes in biological tissues during progressive formalin fixation, Magnetic Resonance in Medicine 79 (2018) 470–478.
[54] P. Hesammokri, Implementation of fractional order viscoelastic models to finite element method, Master's thesis, Middle East Technical University, 2019.
[55] C. Andersson, S. Gedda, J. Åkesson, S. Diehl, Derivative-free parameter optimization of functional mock-up units, in: 9th International Modelica Conference, Modelica Association.
[56] ESTECO, modefrontier - multi objective optimization design environment, 2022. www.esteco.com.
[57] Y.-B. Lu, K. Franze, G. Seifert, C. Steinhäuser, F. Kirchhoff, H. Wolburg, J. Guck, P. Janmey, E.-Q. Wei, J. Käs, A. Reichenbach, Viscoelastic properties of individual glial cells and neurons in the CNS, Proc. Natl. Acad. Sci. U.S.A. 103 (2006) 17759–17764.
[58] M. Pathan, V. Tagarielli, S. Patsias, Effect of fibre shape and interphase on the anisotropic viscoelastic response of fibre composites, Composite Structures 162 (2017) 156–163.
[59] S. Banerjee, B. V. Sankar, Mechanical properties of hybrid composites using finite element method based micromechanics, Composites Part B: Engineering 58 (2014) 318–327.
[60] S. B. R. Devireddy, S. Biswas, Effect of Fiber Geometry and Representative Volume Element on Elastic and Thermal Properties of Unidirectional Fiber-Reinforced Composites, Journal of Composites 2014 (2014) 1–12.
[61] P. Meyer, Bi-logistic growth, Technological Forecasting and Social Change 47 (1994) 89–102.
[62] G. Bertalan, J. Becker, H. Tzschätzsch, A. Morr, H. Herthum, M. Shahryari, R. D. Greenhalgh, J. Guo, L. Schröder, C. Alzheimer, S. Budday, K. Franze, J. Braun, I. Sack, Mechanical behavior of the hippocampus and corpus callosum: An attempt to reconcile ex vivo with in vivo and micro with macro properties, Journal of the Mechanical Behavior of Biomedical Materials 138 (2023) 105613.
[63] N. Reiter, S. Auer, L. Hoffmann, L. Bräuer, F. Paulsen, S. Budday, Do human brain white matter and brain stem structures show direction-dependent mechanical behavior?, Acta Biomaterialia 199 (2025) 230–251.
[64] J. Hou, K. Jiang, A. Ramanathan, A. S. Kumar, W. Zhang, L. Zhao, T. Wu, R. Pidaparti, D. Zhu, G. Li, K. Song, T. Liu, M. J. Razavi, E. Kuhl, X. Wang, Mechanical Characterization of Brain Tissue: Experimental Techniques, Human Testing Considerations, and Perspectives, 2025. Version Number: 2.
[65] M. Bouhrara, R. W. Kim, N. Khattar, W. Qian, C. M. Bergeron, D. Melvin, L. M. Zukley, L. Ferrucci, S. M. Resnick, R. G. Spencer, Age-related estimates of aggregate g -ratio of white matter structures assessed using quantitative magnetic resonance neuroimaging, Human Brain Mapping 42 (2021) 2362–2373.
[66] S. Nicolle, M. Lounis, R. Willinger, J.-F. Palierne, Shear linear behavior of brain tissue over a large frequency range, Biorheology 42 (2005) 209–223.
[67] B. Rashid, M. Destrade, M. D. Gilchrist, Mechanical characterization of brain tissue in tension at dynamic strain rates, Journal of the mechanical behavior of biomedical materials 33 (2014) 43–54.
[68] F. Atashgar, M. Shafieian, N. Abolfathi, From structure to mechanics: exploring the role of axons and interconnections in anisotropic behavior of brain white matter, Biomech Model Mechanobiol 24 (2025) 779–810.
[69] W. Kang, Q. Li, L. Wang, Y. Zhang, P. Xu, Y. Fan, Systematic analysis of constitutive models of brain tissue materials based on compression tests, Heliyon 10 (2024) e37979.
[70] S. Budday, G. Sommer, C. Birkl, C. Langkammer, J. Haybaeck, J. Kohnert, M. Bauer, F. Paulsen, P. Steinmann, E. Kuhl, G. Holzapfel, Mechanical characterization of human brain tissue, Acta Biomaterialia 48 (2017) 319–340.

[71] B. Rashid, M. Destrade, M. D. Gilchrist, Mechanical characterization of brain tissue in simple shear at dynamic strain rates, Journal of the mechanical behavior of biomedical materials 28 (2013) 71–85.
[72] S. Nicolle, M. Lounis, R. Willinger, Shear properties of brain tissue over a frequency range relevant for automotive impact situations: new experimental results, Technical Report, SAE Technical Paper, 2004.
[73] M. C. Murphy, G. L. Curran, K. J. Glaser, P. J. Rossman, J. Huston III, J. F. Poduslo, C. R. Jack Jr, J. P. Felmlee, R. L. Ehman, Magnetic resonance elastography of the brain in a mouse model of alzheimer's disease: initial results, Magnetic resonance imaging 30 (2012) 535–539.
[74] K. Schregel, E. Wuerfel, J. Wuerfel, D. Petersen, R. Sinkus, Viscoelastic properties change at an early stage of cuprizone induced affection of oligodendrocytes in the corpus callosum of c57/black6 mice, in: International Society for Magnetic Resonance in Medicine, volume 2134.
[75] O. Morrison, M. Destrade, B. B. Tripathi, An atlas of the heterogeneous viscoelastic brain with local power-law attenuation synthesised using Prony-series, Acta Biomaterialia 169 (2023) 66–87.
[76] L. Ruhland, N. Reiter, S. Budday, K. Willner, Combining quasi-static and high frequency experiments for the viscoelastic characterization of brain tissue, 2026.
[77] O. Vestrum, Finite Element Implementation of Fibre-Reinforced Materials Model in Abaqus/Explicit, Master's thesis, NTNU, 2015.
[78] P. Liu, X. Li, Dynamic void growth and localization behaviors of glassy polymer using nonlocal explicit finite element analysis, Journal of Peridynamics and Nonlocal Modeling 1 (2019) 3–13.
[79] G. Zheng, N. Zhang, S. Lv, The application of fractional derivative viscoelastic models in the finite element method: taking several common models as examples, Fractal and Fractional 8 (2024) 103.
[80] H. Yuan, X. Xie, A fast fully discrete mixed finite element scheme for fractional viscoelastic models of wave propagation, 2024. Version Number: 5.